Anisotropy characterization of turbulent fluidization

F. Dabbagh ●[1,*] and S. Schneiderbauer ●[1,2,†]

[1]*Christian Doppler Laboratory for Multiscale Modeling of Multiphase Processes, Johannes Kepler University, Altenbergerstraße 69, 4040 Linz, Austria*
[2]*Department of Particulate Flow Modeling, Johannes Kepler University, Altenbergerstraße 69, 4040 Linz, Austria*

This work explores the turbulence anisotropy behavior of a fluidized gas-particle suspension obtained from highly resolved kinetic-theory-based two-fluid model simulations. Therein, the phase-filtered anisotropy Reynolds stress tensor is considered to classify the possible states of turbulence in the barycentric anisotropy invariants map. The temporal turbulence trajectories have revealed a nonlinear converging demarcation line that evolved differently on the gas and solid phases. It isolates the prolate-like cluster's turbulence from the oblate-like background strain on the solid phase, while on the gas phase, the trajectories turn from nearly three-dimensional (3-D) turbulence inside the clusters to 1-D turbulence in the transition regions (from dense to dilute), which then develops into 2-D turbulence in the dilute areas. The converged trajectories at the demarcation lines are found to move always toward isotropy, revealing the return-to-isotropy problem and the tendency to extinguish the bulk anisotropy. The prevalent turbulence type on the solid phase has indicated a 1-D turbulence preference, which is consistent with the reported cluster-induced turbulence in the literature. Moreover, the granular temperature as a quantitative measure of uncorrelated particle agitation is found to accumulate predominantly in 1-D turbulence (dominant solid divergence and strain) and moderately in 2-D turbulence (dominant solid convergence) at the upstream parts of clusters. Similar disclosure of turbulence types is adopted as well, for the variance of solid concentration, drag production, and the magnitudes of the gas-phase Reynolds stress and rate-of-strain tensors. They have demonstrated a similar preferential turbulence anisotropy, which in turn promotes the applicability of the eddy-viscosity approach for modeling the gas-phase Reynolds stress contributions.

I. INTRODUCTION

Any inhomogeneous turbulent single-phase flow at the geometry-dependent large scales tends to return to isotropy at the small scales (the so-called return-to-isotropy [1]) with an equipartitioned energy state through the energy cascade. This phenomenon is characterized by *turbulence anisotropy*. This latter is mainly sustained by turbulent shear stresses (transporting momentum) and the redistribution of energy between Reynolds stress components through the pressure-strain interactions [1]. Studying the anisotropy of turbulence in disperse multiphase flows can be of great interest due to the anomaly of turbulence modulation occurring upon the presence of interphase forces. This means that, in particle-laden turbulent flows, it has been evidenced that the drag force appears as an additional source or sink of the turbulent kinetic energy. The particles therewith

---

*firas.dabbagh@jku.at

†simon.schneiderbauer@jku.at

drain kinetic energy from the carrier fluid at the larger scales, while at a dense cluster shape, they give energy back to the fluid, feeding its turbulent momentum at the small-scale motions [cluster-induced turbulence (CIT)] [2,3]. Investigating anisotropic turbulence, which is potentially relevant to the pressure-rate-of-strain impact (Rotta model [4]), can play a major role into building second-moment models, such as for the Reynolds stresses and turbulent interfacial work. Apart from that, it serves for better understanding of the still ambiguous physics of multiphase turbulence. This widespread physics forms the paradigm of countless applications in environment and industry, such as dynamics in atmospheric cloud and pollutant particles turbulence, sediment transport, debris flows, spray combustion, and pharmaceutical and/or chemical fluidized bed reactors. Analyzing the involved properties helps us to meliorate the design of technological devices and mitigate negative implications of multiphase turbulence, leading to improved turbulence modeling for industrial scale applications.

Anisotropy of turbulence is commonly examined and quantified through the normalized anisotropy Reynolds stress tensor, i.e., the deviatoric (traceless) part of Reynolds stress tensor normalized by turbulent kinetic energy. In fact, simpler than considering all the six independent components of anisotropy tensor, the anisotropy degree and nature are described by only the second *II* and third *III* invariants tensor, in the so-called anisotropy invariant map (AIM) or Lumley triangle [5]. This representation allows a unique mapping of any realizable state of turbulence onto a 2-D nonlinear map spanned by the two invariants. It is introduced as a tool to guide the development of turbulence models analytically, where all turbulent states are bounded inside the invariants space. Any points outside correspond to nonrealizable Reynolds stresses with negative or complex eigenvalues. The AIM has been extensively used to study the trajectories of *II* and *III* invariants in diverse sets of fluid shear and wall-bounded flows. It exposes how the turbulence trajectories evolve from a two-component state at the walls to an axisymmetric near-isotropic state in the bulk center [6]. However, due to the nonlinearity hidden in the invariant definitions, some claims and confusions arise, particularly related to whether the borders of the AIM describe the shape of the stress tensor (energy ellipsoid) or the eddies of turbulence [1]. Moreover, the diagonalization of the anisotropy tensor provides three eigenvalues (magnitudes) and three eigenvectors (directions) of the turbulence anisotropy. The invariants *II* and *III* are only functions of eigenvalues, while ignoring the eigenvectors impedes the information about the directional distribution. Afterward, the anisotropy eigenvalue map introduced by Lumley [7] is utilized to study the anisotropy trajectories in the first and second eigenvalues' linear plane, for different flow configurations [8]. Recently, and as an equivalent linear representation of AIM, the barycentric anisotropy map (BAM) has been proposed by Banerjee *et al.* [6]. The BAM is based on the convex combination of scalar metrics dependent on eigenvalues. It provides a nondistorted visual representation of turbulence anisotropy on an equilateral triangle and more recently with the addition of point-specific color triples [9]. It allows thereby the visualization of turbulence states directly in the physical domain. BAM has been vastly considered in various single-phase flows, as, for instance, in turbulent channel flow [6] and inhomogeneous atmospheric boundary layer turbulence [10], for the analysis of turbulence trajectories. The visual BAM assessment of different Reynolds-averaged Navier-Stokes (RANS) turbulence modeling behavior was employed by Emory and Iaccarino [9] in flows through an urban-like canopy, wavy wall channel, and oblique shock-boundary layer interaction. A main inclusion of BAM framework is, moreover, to quantify the epistemic uncertainties of RANS models by incorporating perturbations to the eigenvalues and the eigenvectors of the modeled Reynolds stress tensor [11]. Each kind of these physical-based perturbations extends the isotropic eddy-viscosity-based model to a general anisotropic eddy-viscosity model [12]. Then, the perturbations lead to a set of different predictions of turbulence quantities, where its union gives an interval estimate of the model uncertainty from the RANS model. Nowadays, machine learning models, for example, the one trained by a random forest model [13], are used to learn the perturbations' magnitude for that eigenspace uncertainty quantification method. This data-driven method has been inspected and advanced for different applications such as flow over a wavy wall and Buice 2-D diffuser [14]. Far from the deep learning and single-phase flows, the BAM has been successfully used to characterize

the anisotropic hemodynamics turbulence in patient-specific cardiovascular flows [15]. It appears as potential method in relevance to blood damage predictions, where RANS turbulence modeling and the 4-D flow MRI (3-D, time-resolved, phase-contrast magnetic resonance imaging) measurements are evaluated against well-resolved large-eddy simulation (LES) results using BAM. Very recently, the BAM has been used to study the effect of the bubbles on the carrier-phase turbulence for vertical channel bubbly flow simulated by direct numerical simulation (DNS) [16]. The authors extend the BAM approach to allow quantification and visualization of anisotropy and componentiality of the flow at any scale. They found that the inclusion of bubbles significantly enhances the anisotropy in the flow at all scales in comparison with the unladen case. In particular, the introduction of small bubbles has strongly increased the intermittency at the dissipation range, but suppressed it at larger scales (similar trends are captured for particle-laden turbulence [2]).

To our best knowledge, no study has explored and characterized the turbulence anisotropy employing BAM in moderately dense gas-solid suspensions. It is a critical space of barycentric coordinates that convey information on the orientation of turbulence and the magnitude of anisotropy [6]. With three limiting borders, BAM classifies the turbulence to 1-D, 2-D isotropic, and 3-D isotropic states, covering any possible state inside its boundaries. Then, following a particular definition of phase stresses, the turbulence shape on that phase can be depicted in any position of the physical domain by a single point in BAM. One of the most feasible numerical methods used to describe particulate flows is the Eulerian continuum approach. Such a method principally treats the particles as interpenetrating continuum, like a fluid, to allow a reliable simulation of turbulent fluidization in large systems. Basically, the domain is discretized into small volumetric units of continuum solid and gas phases, where the interparticle (collisional, dispersion, and rotational) interactions are retrieved basing on the kinetic theory of granular flow [17]. These Eulerian methods are referred to as two-fluid model (TFM) [18,19], and have been shown to properly predict (to a practical, accurate extent) the clustering topology and back-reaction turbulence on sufficiently fine numerical grids [20–22] (resolution on the order of a few particle diameters). In the light of Eulerian similarity, absolute advanced and recent modeling methods for efficient simulations of coupled particle-fluid flows appear to be worth mentioning. For instance, one can recognize the Reynolds-stress modeling proposed by Baker *et al.* [23] applied for the multiphase Reynolds-averaged Navier-Stokes (RANS) [24] TFM in vertical channel particle-laden flows and the sparse regression model closures developed by Beetham *et al.* [25] for the RANS TFM application in homogeneous, fully developed gas-particle flows. On the base of a Lagrangian probability density function (PDF) formalism, the stochastic modeling, served for the TFM development for dense turbulent particle-laden channel flow, was reported by Innocenti *et al.* [26]. In a related aspect, Lattanzi *et al.* [27] developed a force Langevin model that treats neighbor-induced drag fluctuations as a stochastic force within an Eulerian-Lagrangian method. Some other closures were derived as large-eddy simulation type models, using a spatial filtering, as in the dynamic-closured spatially averaged two-fluid model (SA-TFM) [28] and the approximate deconvolution model (ADM-TFM) for moderately dense gas-particle flows [29]. In this paper, nonetheless, and on the basis of highly resolved TFM simulations, we propose to investigate the turbulence anisotropy on the gas and solid phases for a moderately dense fluidized gas-solid suspension. To that end, the phase-filtered anisotropy Reynolds stress tensor is computed on each phase to build the turbulence trajectories in the barycentric anisotropy map. We study a fully periodic (unbounded) fluidization of Geldart type A particles in a cubic box domain. The turbulence trajectories are inquired spatially, as functional of the solid volume fraction, in order to depict the turbulence state from the dilute regions toward inside the clusters. On the other hand, we have identified the turbulence type of essential mechanisms such as the turbulent interfacial work, CIT, solid variance, and granular temperature (pseudo-thermal energy produced by uncorrelated particles' agitation). This study eventually yields to a solid understanding of the underlying physics of turbulence anisotropy driven by the gravity-induced vertical slip, and therefore is a reference for building better models.

The remainder of the paper is organized as follows. A short overview of the numerical TFM simulations adopted for the turbulent fluidization case is given in Sec. II. Then, the theoretical

TABLE I. Summary of main physical properties and simulation parameters for the (unbounded) triply periodic cubic domain of turbulent fluidization studied.

Property	Symbol	Unbounded triply periodic cube
Maximum packing limit	ϵ_s^{max}	0.6
Gas density	ρ_g	1.224 kg m^{-3}
Gas dynamic viscosity	μ_g	1.8×10^{-5} Kg m^{-1} s^{-1}
Internal friction coefficient	μ_i^{st}	0.28
Gravity magnitude	g	9.81 m s^{-2}
Geldart type group		A
Particle density	ρ_s	1500 kg m^{-3}
Particle diameter	d_s	75×10^{-6} m
Terminal settling velocity	u_t	0.22 m s^{-1}
Particle relaxation time	$\tau_s = u_t/g$	0.0224 s
Particle Froude number	Fr $= u_t^2/(d_s g)$	66
Archimedes number	Ar	23
Domain size	$L_x = L_y = L_z$	6 cm
Domain discretization	$N_x \times N_y \times N_z$	$256 \times 256 \times 256$
Grid size	Δ	$3d_s$
Mean particle concentration	$\langle \epsilon_s \rangle$	0.15
Mean mass loading	Φ	216
Cluster length scale	$\mathcal{L}$	$31d_s$
A priori cluster length	$\tau_s^2 g$	$66d_s$

barycentric anisotropy map and relevant turbulence classification are described in Sec. III. Therein, the spatial and temporal turbulence trajectories are inspected on gas and solid phases. Section IV explores the associated physics of the interfacial work and drag production using BAM, while the granular solid temperature is scrutinized in Sec. V. Section VI then outlines the variance solid concentration and drift velocity turbulence anisotropy. Finally, conclusions and future remarks are given in Sec. VII.

II. NUMERICAL METHODS AND TWO-FLUID MODEL

We consider a triply periodic cubic domain to investigate the unbounded fluidization of Geldart A particles. This moderately dense gas-particle flow was simulated using a highly resolved two-fluid model (TFM) employing a sufficiently fine grid good enough to resolve all relevant heterogeneous structures [21,30–32]. The main physical parameters considered, besides the simulation details, are summarized in Table I. A schematic representation of the turbulent fluidization case rendered on an instantaneous solid volume fraction outcome ϵ_s is displayed in Fig. 1(a). Principally, the present case is identical to the turbulent fluidization case considered in Dabbagh and Schneiderbauer [33], holding the same grid size Δ validated but using a different aspect ratio of the box. The TFM approach [34] is adopted employing the classical kinetic theory of granular flows [17]. Namely, considering the gas and solid phases as interpenetrating continua on local mean volumetric units, the solid stresses arising from particle-particle collisions and the translational dispersion of grains are closed by adapting the kinetic theory of gases [17]. In this work, we use consecutive data sets gathered over several time step periods in the statistically stationary flow stage. They ensure a good convergence of qualitative analysis with a minimum sampling number of about 400. Each single datum provides more than 16 millions points information to compute the Reynolds anisotropy tensor and turbulence trajectories, the converged granular temperature, and drag terms in each coordinate (abscissa, ordinate) inside BAM.

Similar to Ref. [33] and for the sake of brevity, the model equations and constitutive relations of dynamics are summarized in Table II. Namely, the Eulerian transport equations of mass, $\rho_l \epsilon_l$,
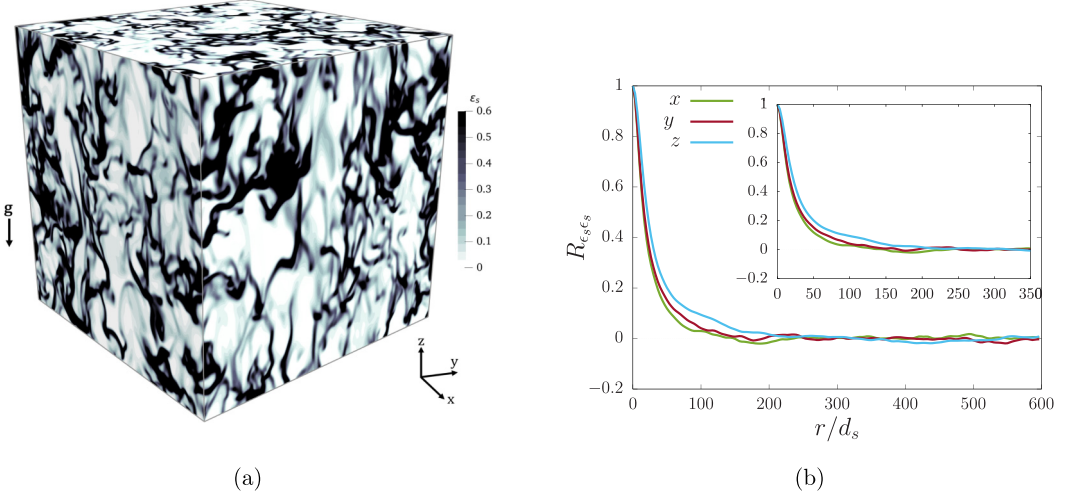
FIG. 1. (a) Schematic representation of the triply periodic cubic domain of turbulent fluidization, rendered on instantaneous ϵ_s outcomes in the TFM simulation. (b) Two-point correlation profiles of ϵ_s, computed in all directions for the studied case, where the inset simply enlarges the statistics to highlight its decay.

momentum, $\rho_l \epsilon_l \boldsymbol{u}_l$, and pseudo-thermal energy Θ_s (on solids) are precisely derived on each phase, l. Therein, ϵ denotes the volume fraction, while ρ and $\boldsymbol{u} = (u, v, w)$ represent the density and velocity field in $\boldsymbol{x} = (x, y, z)$ coordinates, respectively, in correspondence to the subscript gas (g) or solid (s) phase. In dense regions, i.e., where the solid volume fraction is close to maximum packing conditions and the interparticle forces are dominated by long enduring multiple frictional contacts, the solid stress is closed by using an inertial number dependent rheology [35]. The highly resolved TFM simulation is performed using the OpenFOAM (v6) routine with the SuperBee flux limiter [36] for the spatial discretization of convective terms, and least squares method for the derivatives appearing in the diffusion terms. The phasic velocity-pressure coupling was established by the phase-coupling implicit PIMPLE algorithm [37]. For further details about model equations described in Table II, the reader is referred to Ref. [35]. In building the simulation case, a uniform suspension undergoing the infinite fluidization is applied. Namely, on the base of the gravity $\boldsymbol{g} = (0, 0, -g)^t$ body force acting only in the negative vertical z direction, the gas-phase pressure p is adjusted to oppose the body forces and support the weight of the suspension, as

$$-\frac{\partial p}{\partial z} = g[\langle \epsilon_s \rangle \rho_s + (1 - \langle \epsilon_s \rangle) \rho_g], \tag{1}$$

so that no net force acts on the mixture in the z direction. The angle brackets in (1) and hereafter indicate an averaging over the entire domain (likewise, it denotes the ensemble average in the statistical analysis). The number of particles used is determined based on the mean mass loading, given as [38]

$$\Phi = \frac{\rho_s}{\rho_g} \frac{\langle \epsilon_s \rangle}{1 - \langle \epsilon_s \rangle}, \tag{2}$$

where $\langle \epsilon_s \rangle$ is the mean solid concentration (provided in Table I). An important nondimensional number is the Archimedes number, defined as

$$\mathrm{Ar} = \rho_g (\rho_s - \rho_g) \frac{d_s^3 g}{\mu_g^2}. \tag{3}$$

TABLE II. TFM equations for gas-particle flows, similar to those outlined in Ref. [35].

Continuity equation, momentum equation, and transport equation for pseudo-thermal energy [20,34,42]

$$\frac{\partial}{\partial t}\epsilon_g\rho_g + \nabla \cdot (\epsilon_g\rho_g\boldsymbol{u}_g) = 0, \tag{5}$$

$$\frac{\partial}{\partial t}\epsilon_s\rho_s + \nabla \cdot (\epsilon_s\rho_s\boldsymbol{u}_s) = 0, \tag{6}$$

$$\frac{\partial}{\partial t}(\epsilon_g\rho_g\boldsymbol{u}_g) + \nabla \cdot (\epsilon_g\rho_g\boldsymbol{u}_g\boldsymbol{u}_g) = -\epsilon_g\nabla p + \nabla \cdot \epsilon_g\Sigma_g - \beta(\boldsymbol{u}_g - \boldsymbol{u}_s) + \epsilon_g\rho_g\boldsymbol{g}, \tag{7}$$

$$\frac{\partial}{\partial t}(\epsilon_s\rho_s\boldsymbol{u}_s) + \nabla \cdot (\epsilon_s\rho_s\boldsymbol{u}_s\boldsymbol{u}_s) = -\epsilon_s\nabla p - \nabla \cdot \left(\Sigma_s^{kc} + \Sigma_s^{fr}\right) + \beta(\boldsymbol{u}_g - \boldsymbol{u}_s) + \epsilon_s\rho_s\boldsymbol{g}, \tag{8}$$

$$\frac{3}{2}\left(\frac{\partial}{\partial t}(\epsilon_s\rho_s\Theta_s) + \nabla \cdot (\epsilon_s\rho_s\boldsymbol{u}_s\Theta_s)\right) = -\Sigma_s^{kc} : \nabla\boldsymbol{u}_s - \nabla \cdot \boldsymbol{q} + \Gamma_s - J_v - \sigma_{\Theta_s} \tag{9}$$

Interphase momentum exchange [39]

$$\beta = \frac{3}{4}C_D\frac{\epsilon_g\epsilon_s\rho_g\|\boldsymbol{u}_g - \boldsymbol{u}_s\|}{d_s}\epsilon_g^{-2.65}$$

$$\text{with} \quad C_D = \begin{cases} \frac{24}{\text{Re}_s}[1 + 0.15\text{Re}_s^{0.687}] & \text{Re}_s < 1000 \\ 0.44 & \text{Re}_s \geqslant 1000 \end{cases} \qquad \text{Re}_s = \frac{\epsilon_g\rho_g d_s\|\boldsymbol{u}_g - \boldsymbol{u}_s\|}{\mu_g} \tag{10}$$

Gas-phase and solid-phase stress tensors

$$\Sigma_g = 2\mu_g\mathsf{S}_g, \quad \Sigma_s^{kc} = \left(p_s^{kc} - \lambda_s^{kc}tr(\mathsf{S}_s)\right)\mathsf{I} - 2\mu_s^{kc}\mathsf{S}_s^d, \quad \Sigma_s^{fr} = 2\mu_s^{fr}\mathsf{S}_s - p_s^{fr}\mathsf{I}$$

$$\mathsf{S}_l = \frac{1}{2}(\nabla\boldsymbol{u}_l + (\nabla\boldsymbol{u}_l)^t), \quad \mathsf{S}_s^d = \mathsf{S}_s - \frac{1}{3}tr(\mathsf{S}_s)\mathsf{I} \tag{11}$$

Radial distribution function

$$g_0 = \frac{1}{1 - \left(\epsilon_s/\epsilon_s^{\text{mas}}\right)} \tag{12}$$

Solid viscosity ($\mathbb{L}$ is the characteristic length scale of actual physical system and is set to the height of domain)

$$\mu_s^{kc} = \left(\frac{2+\alpha}{3}\right)\left\{\frac{\mu^*}{g_0\eta_s(2 - \eta_s)}\left(\frac{1}{1 + \frac{l_s}{\mathbb{L}}} + \frac{8}{5}\epsilon_s\eta_s g_0\right)\left(1 + \frac{8}{5}\eta_s(3\eta_s - 2)\epsilon_s g_0\right) + \frac{3}{5}\eta_s\mu_b\right\}$$

$$\mu^* = \frac{\mu}{1 + \frac{2\beta\mu}{(\epsilon_s\rho_s)^2 g_0\Theta_s}}, \quad \mu = \frac{5\rho_s d_s\sqrt{\pi\Theta_s}}{96}, \quad \mu_b = \frac{256\mu\epsilon_s^2 g_0}{5\pi}, \tag{13}$$

$$\alpha = \frac{8}{5}, \quad \eta_s = \frac{1}{2}(1 + e_s), \quad l_s = \frac{d_s}{6\sqrt{2}g_0\epsilon_s}$$

TABLE II. *(Continued.)*

pseudo-thermal energy (PTE) flux vector $\boldsymbol{q} = \kappa \nabla \Theta_s$, rate of dissipation of PTE σ_{Θ_s}, rate of dissipation of PTE by viscous damping J_v, and rate of production of PTE by gas-particle slip Γ_s

$$\boldsymbol{q} = -\frac{\kappa^*}{g_0} \left\{ \left(\frac{1}{1 + \frac{l_s}{\mathbb{L}}} + \frac{12}{5} \eta_s \epsilon_s g_0 \right) + \left(1 + \frac{12}{5} \eta_s^2 (4\eta_s - 3) \epsilon_s g_0 \right) + \frac{64}{25\pi}(41 - 33\eta_s)\eta_s^2 \epsilon_s^2 g_0^2 \right\} \nabla \Theta_s,$$

$$\sigma_{\Theta_s} = \frac{48}{\sqrt{\pi}} \eta_s (1 - \eta_s) \frac{\rho_s \epsilon_s^2}{d_s} g_0 \Theta_s^{3/2}, \quad \kappa^* = \frac{\kappa}{1 + \frac{6\beta\kappa}{5(\epsilon_s \rho_s)^2 g_0 \Theta_s}},$$

$$\kappa = \frac{75 \rho_s d_s \sqrt{\pi \Theta_s}}{48 \eta_s (41 - 33\eta_s)}, \quad \Gamma_s = \frac{d_s \beta^2 \|\boldsymbol{u}_g - \boldsymbol{u}_s\|^2}{4 \epsilon_s g_0 \rho_s \sqrt{\pi \Theta_s}} \Psi,$$

$$J_v = \frac{54 \epsilon_s \mu_g \Theta_s}{d_s^2} R_{\text{diss}}, \quad \text{where } \Psi \text{ and } R_{\text{diss}} \text{ are given in Eqs. (51) and (52), following Ref. [20]} \tag{14}$$

Solid pressure and bulk viscosity

$$p_s^{kc} = \epsilon_s \rho_s \left(\frac{1}{1 + \frac{l_s}{\mathbb{L}}} + 4\eta_s \epsilon_s g_0 \right) \Theta_s, \quad \lambda_s^{kc} = \frac{8}{3} \eta_s \epsilon_s^2 \rho_s d_s g_0 \sqrt{\frac{\Theta_s}{\pi}} \tag{15}$$

Frictional pressure and viscosity [35] ($b \approx 0.2$, $I_0 = 0.279$, $\mu_i^{st} = \tan(20.9°)$, $\mu_i^c = \tan(32.76°)$)

$$p_s^{fr} = 4\rho_s \left(\frac{b d_s \sqrt{\mathsf{S}_s : \mathsf{S}_s/2}}{\epsilon_s^{max} - \epsilon_s} \right)^2, \quad \mu_s^{fr}(I_s, p_s^{fr}, \mathsf{S}_s) = \frac{\mu_i(I_s) p_s^{fr}}{2\sqrt{\mathsf{S}_s : \mathsf{S}_s/2}},$$

$$\mu_i(I_s) = \mu_i^{st} + \frac{\mu_i^c - \mu_i^{st}}{\frac{I_0}{I_s} + 1}, \quad I_s = \frac{2 d_s \sqrt{\mathsf{S}_s : \mathsf{S}_s/2}}{\sqrt{p_s^{fr}/\rho_s}} \tag{16}$$

Alternatively, a Froude number is introduced to characterize the balance between gravitational and inertial forces, defined as $\text{Fr} = u_t^2/(d_s g)$, where u_t is the terminal settling velocity computed used Wen and Yu drag [39]. Another important quantity is the characteristic cluster length scale, which can be estimated *a priori* as $\tau_s^2 g$ [20,38,40], where $\tau_s = u_t/g$ is the particle relaxation time (or drag time). An accurate value of the characteristic cluster length scale, $\mathcal{L}$, can be measured *a posteriori* by computing the two-point correlation of ϵ_s in the three-direction domain. Namely, the two-point correlation formulas given by

$$R_{\epsilon_s \epsilon_s} = \frac{\langle \epsilon_s'(\boldsymbol{x}) \epsilon_s'(\boldsymbol{x} + r) \rangle}{\langle \epsilon_s'^2 \rangle} \tag{4}$$

are plotted in all three directions in Fig. 1(b). $\langle \epsilon_s'^2 \rangle$ in Eq. (4) implies the temporal variance of ϵ_s, and by taking the integral of the two-point correlation curves, i.e., $\int R_{\epsilon_s \epsilon_s} dr$ (commencing from 1 till the first zero decay), we obtain the cluster length scale $\mathcal{L}$, given in Table I. The two-point correlation values, on the other hand, assure the domain size adequacy, where all profiles in Fig. 1(b) fall to zero at separations less than one-half distance. At the end, it is worth mentioning that the resolution results using the kinetic-theory-based TFM have been previously validated by Dabbagh and Schneiderbauer [33]. Therein, as mentioned above, an unbounded periodic box turbulent fluidization is adopted, while we use here identical grid size Δ and simulation parameters (same mass loading) in a triply periodic cubic domain. The prediction for the slip velocity defined as

the absolute difference global and phase-averaged streamwise phase velocities [21] yields a value of 0.25 m/s, which is nearly indistinguishable from the value of TFM simulations reported by Fullmer and Hrenya [21] using MFIX (at the same mass loading). Moreover, our slip velocity value is quite comparable with the 0.29 m/s result using Eulerian-Lagrangian simulations by Radl and Sundaresan [41] (at the same mass loading). It is notable that the box employed in Ref. [41] is about 2–8 times smaller than our cubic domain, which in turn shows a good convergence for the cluster size [Fig. 1(b)].

III. ANISOTROPY STRESS TENSOR AND BARYCENTRIC MAP

We consider a phase-filtered Reynolds stress tensor, i.e., spatially filtered and phase averaged (PA), as a measure of a phase-weighted local ensemble correlation of two fluctuating velocities. Therefore, by defining a volumetric mean or locally averaged filter for any field variable as $\overline{\xi}(\boldsymbol{x}, t) = \int_V G_{\bar{\Delta}}(\boldsymbol{x}, \boldsymbol{x}', \bar{\Delta})\xi(\boldsymbol{x}', t)dV_{\boldsymbol{x}'}$, with a weighting function $G_{\bar{\Delta}}(\boldsymbol{x}, \boldsymbol{x}', \bar{\Delta})$ satisfying $\int_V G_{\bar{\Delta}}(\boldsymbol{x}, \boldsymbol{x}', \bar{\Delta})dV_{\boldsymbol{x}'} = 1$, then the phase average analogous to Favre averaging in variable density flow can be written as

$$\langle \xi \rangle_l = \frac{\overline{\epsilon_l \xi}}{\overline{\epsilon_l}}, \tag{17}$$

where l is the phase notation (solid or gas). Subsequently, the subfilter fluctuations are

$$\xi' = \xi - \overline{\xi}, \tag{18}$$

$$\boldsymbol{u}_g''' = \boldsymbol{u}_g - \langle \boldsymbol{u}_g \rangle_g, \quad \text{about PA gas velocity.} \tag{19}$$

$$\boldsymbol{u}_s'' = \boldsymbol{u}_s - \langle \boldsymbol{u}_s \rangle_s, \quad \text{about PA solid velocity.} \tag{20}$$

The phase-filtered Reynolds stress tensors are then given on each phase by

$$\langle \boldsymbol{u}_s'' \otimes \boldsymbol{u}_s'' \rangle_s = \langle \boldsymbol{u}_s \otimes \boldsymbol{u}_s \rangle_s - \langle \boldsymbol{u}_s \rangle_s \otimes \langle \boldsymbol{u}_s \rangle_s, \tag{21}$$

$$\langle \boldsymbol{u}_g''' \otimes \boldsymbol{u}_g''' \rangle_g = \langle \boldsymbol{u}_g \otimes \boldsymbol{u}_g \rangle_g - \langle \boldsymbol{u}_g \rangle_g \otimes \langle \boldsymbol{u}_g \rangle_g. \tag{22}$$

The trace of Eqs. (21) and (22) are twice the turbulent kinetic energy, i.e.,

$$2k_s = \langle \boldsymbol{u}_s'' \cdot \boldsymbol{u}_s'' \rangle_s = \langle \boldsymbol{u}_s \boldsymbol{u}_s \rangle_s - \langle \boldsymbol{u}_s \rangle_s \langle \boldsymbol{u}_s \rangle_s, \tag{23}$$

$$2k_g = \langle \boldsymbol{u}_g''' \cdot \boldsymbol{u}_g''' \rangle_g = \langle \boldsymbol{u}_g \boldsymbol{u}_g \rangle_g - \langle \boldsymbol{u}_g \rangle_g \langle \boldsymbol{u}_g \rangle_g, \tag{24}$$

indicating the intensity of turbulence, while the off-diagonal components are responsible for transporting momentum by the turbulence anisotropy. The anisotropy stress tensors are defined as the deviatoric (traceless) part of Reynolds stress tensors normalized by twice the turbulent kinetic energies [7], as follows:

$$\mathsf{B}_s = \frac{\langle \boldsymbol{u}_s'' \otimes \boldsymbol{u}_s'' \rangle_s}{2k_s} - \frac{1}{3}\mathsf{I}, \tag{25}$$

$$\mathsf{B}_g = \frac{\langle \boldsymbol{u}_g''' \otimes \boldsymbol{u}_g''' \rangle_g}{2k_g} - \frac{1}{3}\mathsf{I}, \tag{26}$$

where I is Kronecker's delta. Since the Reynolds stress tensor is a symmetric, second-order, and positive semi-definite matrix (its individual components satisfy the physical realizability constraints [43]), the anisotropy stress tensor is also symmetric and can be diagonalized by real eigenvalues $\lambda_{\boldsymbol{b}_1} \geqslant \lambda_{\boldsymbol{b}_2} \geqslant \lambda_{\boldsymbol{b}_3} \in [-1/3, 2/3]$ and eigenvectors $\{\boldsymbol{b}_1, \boldsymbol{b}_2, \boldsymbol{b}_3\}$ associated with each eigenvalue, to be mutually orthogonal. Then, from the spectral decomposition theorem, the anisotropy stress tensor
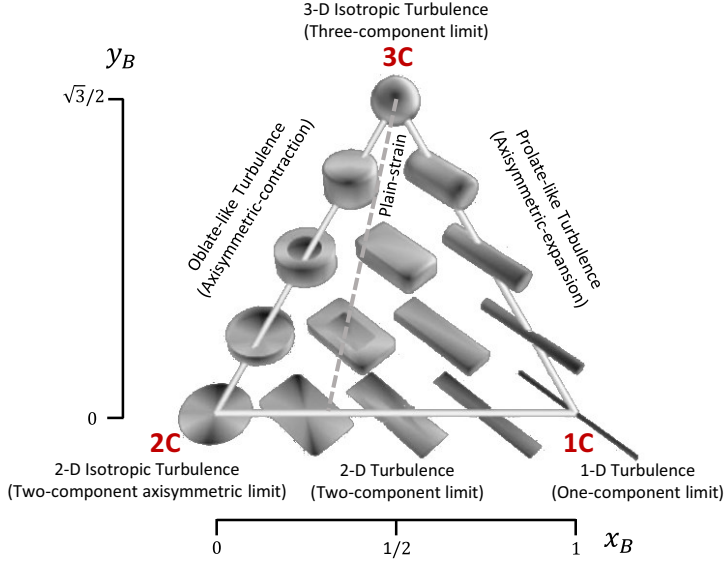
FIG. 2. Barycentric anisotropy map (BAM) based on scalar metrics which are functions of eigenvalues of the second-order anisotropy stress tensor describing turbulence. It characterizes the shape of energy ellipsoid (turbulence componentiality) with three limiting states $\{C_{1C}, C_{2C}, C_{3C}\}$, representing the vertices of an equilateral triangle classification. The isotropic point has a metric $C_{3C} = 1$, the two-component point has $C_{2C} = 1$, and the one-component point has $C_{1C} = 1$. Any physically realizable state of turbulence must lie inside this triangle. The shapes of turbulence classified are therein described together with super-quadratic tensor glyphs visualization [44] taken from Ref. [45].

can be written in canonical form as [6]

$$\tilde{\mathsf{B}} = \lambda_{b_1} b_1 b_1^t + \lambda_{b_2} b_2 b_2^t + \lambda_{b_3} b_3 b_3^t. \tag{27}$$

The degree and nature of anisotropy are characterized by the second II and third III invariants of B identified as functions of the anisotropy eigenvalues,

$$II = \frac{tr(\mathsf{B}^2)}{2} = \lambda_{b_1}^2 + \lambda_{b_1}\lambda_{b_2} + \lambda_{b_2}^2, \quad III = \frac{tr(\mathsf{B}^3)}{3} = -\lambda_{b_1}\lambda_{b_2}(\lambda_{b_1} + \lambda_{b_2}). \tag{28}$$

They represent a relative strength of different fluctuating velocity components, referred to as turbulence componentiality [9], and compose the two-coordinate system (III, II) into the bounded anisotropy invariant map (AIM) or Lumley triangle [5]. All physically realizable states of turbulence must lie inside this map limited by three states at the corners. Namely, based on the shape of energy ellipsoid or the componentiality of turbulence, the ellipsoid's major, medium, and minor axes are along the $\tilde{\mathsf{B}}$ eigenvectors, with scaling factors being the eigenvalues. Then, the rank or the nonzero eigenvalues of $\tilde{\mathsf{B}}$ can reflect three fundamental limiting turbulence states [5,6] (see Fig. 2 in barycentric anisotropy map representation):

(1) *One-component limit (1C)*. It corresponds to one-rank tensor $\tilde{\mathsf{B}}$ with $\lambda_{b_1} > 0 > \lambda_{b_2} \approx \lambda_{b_3}$. The turbulence is only one-component of the turbulent kinetic energy (1-D turbulence) acting along one direction b_1. The basis matrix of anisotropy tensor for this limiting state is given by

$$\tilde{\mathsf{B}}_{1C} = \begin{pmatrix} 2/3 & 0 & 0 \\ 0 & -1/3 & 0 \\ 0 & 0 & -1/3 \end{pmatrix}. \tag{29}$$

(2) *Two-component axisymmetric limit (2C).* It corresponds to two-rank tensor $\tilde{\mathsf{B}}$ where $\lambda_{b_1} \approx \lambda_{b_2} > 0 > \lambda_{b_3}$. The turbulence is two-component isotropic (2-D isotropic turbulence), where one component of the turbulent kinetic energy vanishes with the remaining two being equal. It acts uniformly in a plane spanned by the two eigenvectors b_1 and b_2. The basis matrix of anisotropy tensor for this limiting state is given by

$$\tilde{\mathsf{B}}_{2C} = \begin{pmatrix} 1/6 & 0 & 0 \\ 0 & 1/6 & 0 \\ 0 & 0 & -1/3 \end{pmatrix}. \tag{30}$$

(3) *Three-component limit (3C).* It corresponds to three-rank tensor $\tilde{\mathsf{B}}$ where $\lambda_{b_1} = \lambda_{b_2} = \lambda_{b_3}$. The turbulence is three-component isotropic (3-D isotropic turbulence) acting randomly in a sphere; the axes of sphere are spanned by the eigenvectors b_1, b_2, and b_3. The basis matrix of anisotropy tensor for this limiting state is given by

$$\tilde{\mathsf{B}}_{3C} = \begin{pmatrix} 0 & 0 & 0 \\ 0 & 0 & 0 \\ 0 & 0 & 0 \end{pmatrix}. \tag{31}$$

The borders between these limiting states are described by a mix of intermediate characteristics:

(1) *Two-component limit* connects 1C and 2C and represents an ellipse planer-like 2-D turbulence.

(2) *Axisymmetric expansion* connects 1C and 3C and represents a prolate-like turbulence.

(3) *Axisymmetric contraction* connects 2C and 3C and represents an oblate-like turbulence.

(4) *Plane-strain limit.* Along this line one anisotropy eigenvalue λ_{b_i} is zero except at 3C, and the mean momentum exchange due to turbulent fluctuation only occurs along a plane.

Hence, the anisotropy tensor $\tilde{\mathsf{B}}$ [Eq. (27)] can be expressed as a convex combination of the three limiting states (1C, 2C, 3C) [6] as

$$\tilde{\mathsf{B}} = C_{1C}\tilde{\mathsf{B}}_{1C} + C_{2C}\tilde{\mathsf{B}}_{2C} + C_{3C}\tilde{\mathsf{B}}_{3C}, \tag{32}$$

where $\{C_{1C}, C_{2C}, C_{3C}\}$ are the coordinates of the anisotropy tensor $\tilde{\mathsf{B}}$ in the tensor basis $\{\tilde{\mathsf{B}}_{1C}, \tilde{\mathsf{B}}_{2C}, \tilde{\mathsf{B}}_{3C}\}$. To obtain a measure of anisotropy from the anisotropy tensor $\tilde{\mathsf{B}}$, metrics of three different kinds of anisotropy are provided in a normalizing manner, such that

$$C_{1C} + C_{2C} + C_{3C} = 1, \tag{33}$$

where C_{1C} is a linear measure of anisotropy and C_{2C} is the planar measure of anisotropy. The normalization is done in such a way that all metrics $\{C_{1C}, C_{2C}, C_{3C}\}$ are in the range [0,1]. It is worth noting that $\tilde{\mathsf{B}}_{3C}$ is a null matrix which can make Eq. (32) nonunique but the restriction on C_{3C} using Eq. (33) forces it to be unique. Thus, by setting

$$C_{1C} = \lambda_{b_1} - \lambda_{b_2}, \tag{34}$$

$$C_{2C} = 2\big(\lambda_{b_2} - \lambda_{b_3}\big), \tag{35}$$

$$C_{3C} = 3\lambda_{b_3} + 1, \tag{36}$$

an equilateral triangle barycentric anisotropy map (BAM) can be constructed to characterize turbulence within the three limiting states (1C, 2C, 3C) representing the three vertices of this map [6]. Note that Fig. 2 displays the BAM with all turbulence state descriptions together with superquadratic tensor glyphs visualization [44] taken from Ref. [45]. At each vertex, one of the metrics $\{C_{1C}, C_{2C}, C_{3C}\}$ has a value of 1 to express the normalized weight of anisotropy nature. Any point inside the map has local coordinates $\{C_{1C}, C_{2C}, C_{3C}\}$, which help to know directly the weighting of the three limiting states of turbulence. The BAM is then plotted in an Euclidean space where the

limiting states are placed at $(x_{1C}, y_{1C}) = (1, 0)$, $(x_{2C}, y_{2C}) = (0, 0)$ and $(x_{3C}, y_{3C}) = (1/2, \sqrt{3}/2)$, and the coordinates system (x_B, y_B) are defined such that

$$x_B = C_{1C}x_{1C} + C_{2C}x_{2C} + C_{3C}x_{3C} = C_{1C} + \frac{1}{2}C_{3C} = \lambda_{b_1} - \lambda_{b_2} + \frac{1}{2}(3\lambda_{b_3} + 1), \qquad (37)$$

$$y_B = C_{1C}y_{1C} + C_{2C}y_{2C} + C_{3C}y_{3C} = \frac{\sqrt{3}}{2}C_{3C} = \frac{\sqrt{3}}{2}(3\lambda_{b_3} + 1). \qquad (38)$$

The plane-strain line function is thus defined as

$$y_{ps} = 6\left(x_{ps} - \frac{1}{2}\right) + \frac{\sqrt{3}}{2}. \qquad (39)$$

In contrast to the Lumley triangle [5], the barycentric map conveys information on the orientation of turbulence and magnitude of anisotropy and does not introduce any visual bias of the limiting states (1C, 2C, 3C), which are located equidistantly on the vertices triangle [6].

Now, we inspect the classification of turbulence states in BAM using the highly resolved TFM simulation data for moderately dense (gas-particle) turbulent fluidization case. Taking the solid phase, the phase-filtered anisotropy stress tensor [Eq. (25)] is computed about a filter length $\bar{\Delta} = 3\Delta < \mathcal{L}$ smaller than the cluster size to ensure disclosing the underlying turbulence structures inside clusters. Note that the spatial filtering can imply a similar picture to the temporal averaging (ensemble time-averaged fluctuating velocity correlation used to study the anisotropy in the single-phase literature); here we exclude the weighted-phase fluctuations about a filter length and ensemble them locally and temporally (using multiple snapshots) in the constraint of BAM. Namely, we perform a statistical analysis for the turbulence anisotropy by evaluating the joint probability density function (JPDF) of the scalar metrics x_B and y_B in BAM [Eqs. (37) and (38)], based on the solid-filtered anisotropy stress tensor [Eq. (25)], utilizing multiple snapshots. The most dominant turbulence state on solids dynamics shows a 1-D turbulence type, as demonstrated in Fig. 3(a). It arises from the slip velocity acting vertically in the gravity direction to suspend the particles by drag, and makes the vertical z component of turbulent kinetic energy prevalent. This can be a remarkable signature on the turbulence anisotropy driven essentially by the streamwise component of phase Reynolds stress tensor in gravity-driven CIT, reported consistently in the literature [25,26,46,47]. For instance, Ferrante and Elghobashi [48] show that the fluid flow crossing large particles through turbulent eddies creates local gradients in the fluid due to particle drag and causes the turbulence to become anisotropic, with turbulent kinetic energy level always higher as compared to unladen case. It is worth mentioning that similar trends of turbulence preference are found on the gas phase (due to the gas-solid interaction) but not shown here. On the other hand, the use of wider filter length does not influence the essential turbulence distribution on BAM. It only makes the picture tend toward 3C because of the inclusion and enlargement of solid slots. The JPDF (x_B, y_B) gave a qualitative statistical image of the predominant turbulence state over the entire domain and involved dynamics; nonetheless, identifying the anisotropy in particular regions can be of more interest. To that end, we investigate the turbulence trajectories, changed spatially and colored by the solid volume fraction, in order to depict the turbulence state from dilute regions toward inside the clusters. Namely, we assemble the values of (x_B, y_B) (from space and time) in each bin width for the solid volume fraction and plot it as a point in BAM. Considering both phases, the resulting spatial turbulence trajectories are rendered in Figs. 3(b) and 3(c), for the gas and solid phases, respectively, where the color bar follows the value of $\bar{\epsilon}_s$. They evolve differently; the gas-phase turbulence is essentially 2-D planer-like in the dilute regions, altering to 1-D turbulence in transition areas and going upward to 3-D turbulence (elongated pancake-like) at the interface and inside the clusters (cluster limits assumed by $\bar{\epsilon}_s \in [0.3, 0.6]$). This observation agrees well with our reported findings in Ref. [33], showing that the gas-phase flow topology in moderately dense turbulent fluidization presents a strong tendency to the boundary-layer-like 2-D turbulence. The solid-phase scenario nonetheless, is different, starting from $\bar{\epsilon}_s = 0.05$ where the turbulence trajectories are identified 1-D turbulence, and
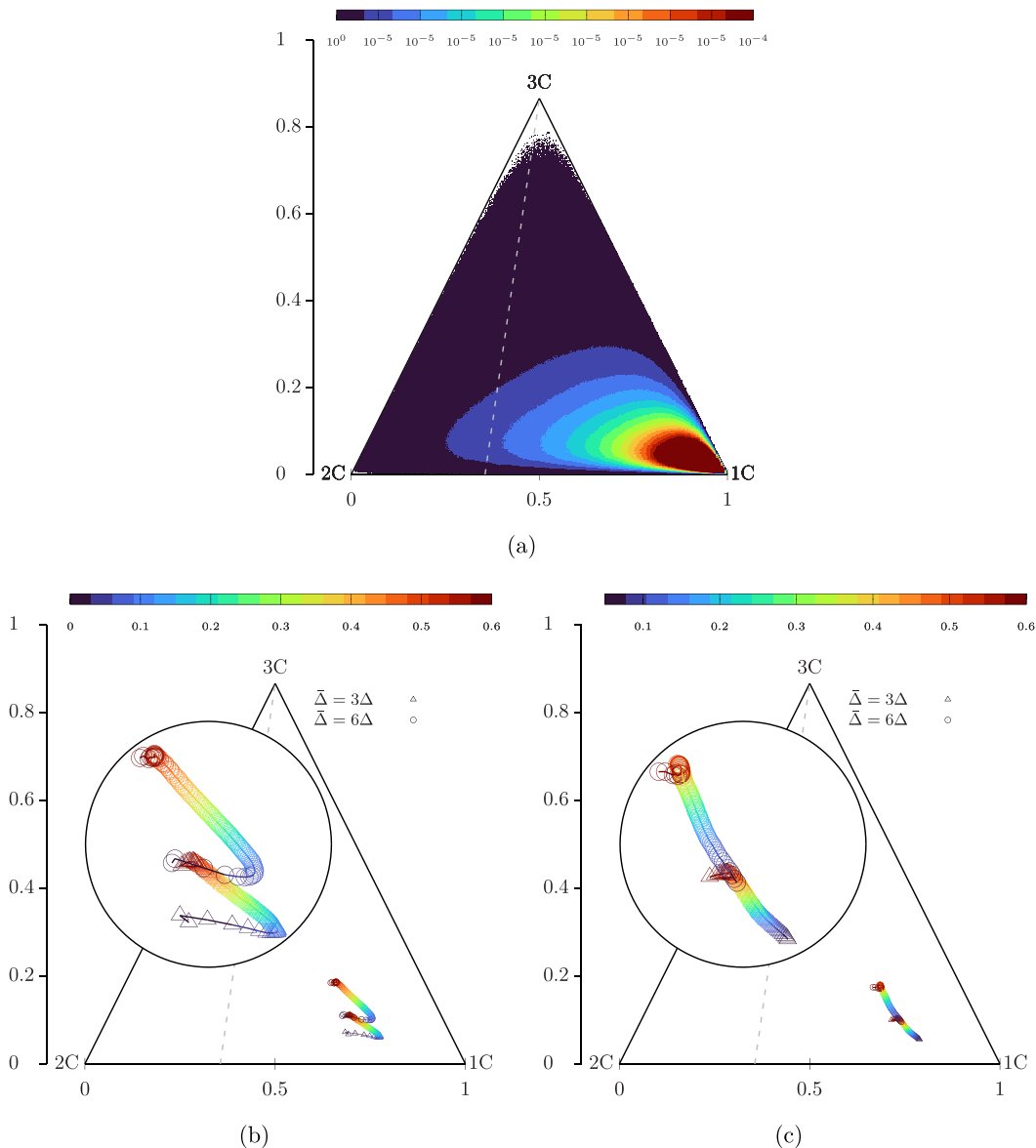
FIG. 3. (a) JPDF of (x_B, y_B) coordinates in BAM, corresponding to the solid-phase-filtered anisotropy stress tensor [Eq. (25)] with $\bar{\Delta} = 3\Delta$. (b) displays the gas-phase turbulence trajectories in BAM, changed spatially as functional to $\bar{\epsilon}_s$ (varying color), and using two filter lengths $\bar{\Delta} = \{3\Delta, 6\Delta\}$ (varying symbol). (c) shows the solid-phase turbulence trajectories as in (b). All trajectories are enlarged in a circle subset, and the data are taken from the TFM turbulent fluidization case.

move directly upward in prolate-like toward 3-D turbulence at the interface and inside the clusters. Two filter lengths are investigated in the bounds of clusters size, i.e., $\bar{\Delta} = \{3\Delta, 6\Delta\} < \mathcal{L} \sim 10\Delta$, and revealed no impact on the turbulence trajectories behavior; this latter only goes upward at wider filter, creeping toward 3C because of the smearing effect.

Another important insight into the turbulence anisotropy can be obtained from studying its decaying evolution. Meaning, if we analyze the material derivative of $\tilde{B}$, one can get trajectories
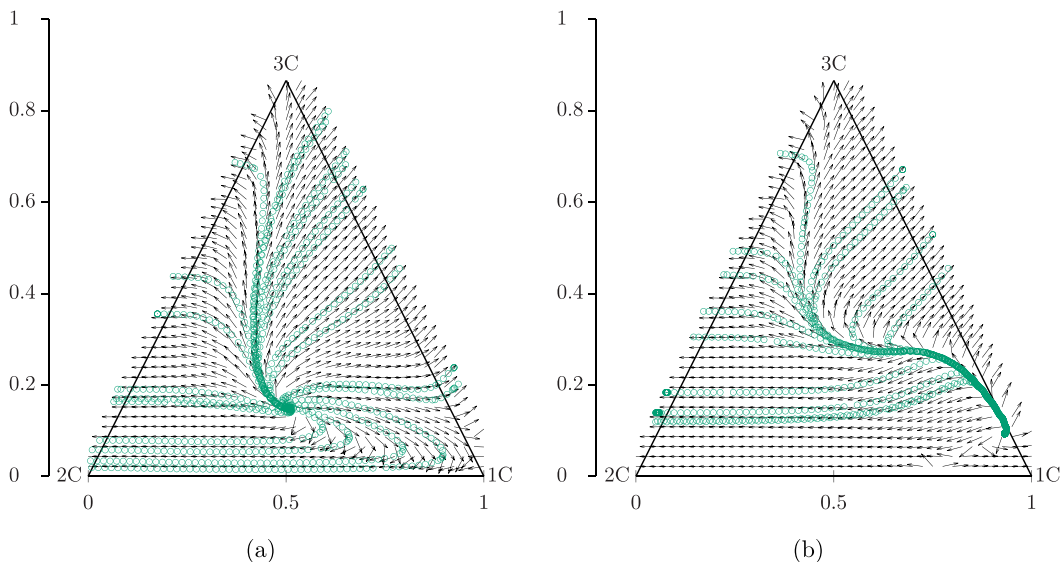
FIG. 4. Conditional mean vectors of $\langle Dx_B/Dt \rangle$ and $\langle Dy_B/Dt \rangle$ in (x_B, y_B) BAM together with some integral trajectories (green circles) and $\bar{\Delta} = 3\Delta$. They inspect the temporal turbulence trajectories or rate of return-to-isotropy on the gas (a) and solid (b) phases of the TFM turbulent fluidization case.

within the Lumley triangle [5], revealing the rate of return-to-isotropy [49] for decaying homogeneous single-phase turbulence. Therefore, in this work, we decide to look at the evolution of scalar metric x_B and y_B in BAM, to unveil how the states of turbulence change over time in the frame of a moving observer following a phase parcel. Namely, taking the Lagrangian derivatives, $Dx_B/Dt = (\partial x_B/\partial t) + (\langle \boldsymbol{u} \rangle_l \cdot \nabla)x_B$ and $Dy_B/Dt = (\partial y_B/\partial t) + (\langle \boldsymbol{u} \rangle_l \cdot \nabla)y_B$, we compute the mean trajectories $(\langle Dx_B/Dt \rangle, \langle Dy_B/Dt \rangle)$, yielding 2-D vectors conditioned by (x_B, y_B) space or BAM constraint. These vectors are plotted in Figs. 4(a) and 4(b) for the gas and solid phases, respectively. The converging vectors are found to be placed at the demarcation lines, while all vectors are uniformly rendered and normalized by their own magnitude. Some trajectories are incorporated as green circles to enhance the streamlines capturing. In principle, and as can be seen from Fig. 4(a), the turbulence trajectories on the gas phase reveal almost a rotating behavior centralized in the lower part of BAM. They read that any prolate-like 3-D turbulence interacting or colliding with clusters develops to 1-D turbulence and then to 2-D turbulence to continue toward disk-like or proceed developing toward 3-D turbulence following the demarcation line and driven by the clusters. The turbulence trajectories on solid phase [Fig. 4(b)], however, show a clear demarcation line that isolates any prolate-like cluster's turbulence which develops to 3-D isotropic, from any oblate-like background strain on solids which develops to 2-D disk-like or pancake-like turbulence.

Our decaying evolution might depart principally from the linear Rotta model [4] or the nonlinear Sarkar-Speziale model [50] for the return-to-isotropy problem. These models give a representation of the slow pressure-strain correlation term as a function of the anisotropy stress tensor and viscous dissipation. They make use of vanishing the rapid part of pressure-strain correlation by removing the velocity gradients in a *decaying, homogeneous anisotropic turbulence*, meaning that the shear production and diffusive transport are neglected in the transport equation of Reynolds stress tensor, and any initial turbulence anisotropy will relax toward isotropy. The evolution of anisotropy stress tensor is then written in terms of the viscous dissipation, turbulent kinetic energy, the tensor itself, and its invariants (II, III) [50]. For any initial anisotropy state expanded between 1C and 2C in the phase space AIM (II, III), a nonlinear trajectory can be built by resolving the evolution transport of II and III (or $\xi^3 = (-1/2)\lambda_{\boldsymbol{b}_1}\lambda_{\boldsymbol{b}_2}(\lambda_{\boldsymbol{b}_1} + \lambda_{\boldsymbol{b}_2})$ and $\eta^2 = (1/3)(\lambda_{\boldsymbol{b}_1}^2 + \lambda_{\boldsymbol{b}_1}\lambda_{\boldsymbol{b}_2} + \lambda_{\boldsymbol{b}_2}^2)$, in the

Sarkar-Speziale model [50]), relaxing to 3C. In fact, our initial anisotropy state is only one spatially phase-filtered map which might be represented as one starting point trajectory in the Sarkar-Speziale model (if we integrate over the whole domain). But, we have starting points for trajectories every where in BAM and we append more moments, averaging in time to get a converged set of trajectories at the demarcation lines. Note that the demarcation line in Fig. 4 on both gas and solid phases is nonlinear and always moves toward 3C to indicate the smearing effect for cluster's turbulence. We might consider it as a tendency to extinguish the bulk anisotropy as originally conceived by Rotta [4] (thus the label return-to-isotropy may be adopted here). Sampling more moments is like using wider filter lengths and the cluster's turbulence or the gas turbulence parcels driven by the clusters become more prolate-like toward 3C. If we compare our converging demarcation lines with the trajectory points obtained by Stiperski *et al.* [10], who use clustered data from atmospheric boundary layer turbulence at different bulk anisotropy, one can notice a close behavior of the gas-phase demarcation points to the two-component bulk anisotropy trajectories, whereas the solid-phase demarcation points might close the one-component bulk anisotropy trajectory. Notably, our turbulent fluidization is not a decaying turbulence and none of the budget terms can be ignored. Thus, the nonlinear return-to-isotropy models, such as Sarkar-Speziale, are not comparable to our trajectories (Fig. 4), precisely as reported by Stiperski *et al.* [10]. Therein, all atmospheric surface layer turbulence trajectories were found to depart significantly from those of Ref. [50], particularly the two- and one-component turbulence, in (ξ, η) AIM. At the end, our trajectories reveal a rate of change for nonrelaxing turbulence induced by a gravity-driven gas-particle coupled flow.

IV. INTERFACIAL WORK AND CLUSTER-INDUCED TURBULENCE

The key complexity of disperse (particle-laden) multiphase flows arises from the interfacial momentum coupling between particles and the carrier fluid. More precisely, when the particles mass loading in the flow is sufficiently high and subject to a mean force (e.g., gravity), the particles tend to organize into dense clusters due to the nonlinear drag force [20]. In statistically station-ary conditions, the fluctuations in the particle concentration and fluid velocity can generate and sustain fluid-phase turbulence (pseudo-turbulence), which is referred as cluster-induced turbulence (CIT), even in the absence of mean shear [46]. In this context, we aim to depict the inherent turbulence state corresponding to the essential mechanisms of turbulent interfacial work (drag-dissipation-and-exchange) and CIT production [38,46]. Following previous studies [24,38,46,51–53], the microscopic drag coefficient divided by the solid volume fraction can be approximated by the zeroth-order Taylor series expansion about the filtered components, i.e., $(\overline{\epsilon}_s, \langle \boldsymbol{u}_g \rangle_g, \langle \boldsymbol{u}_s \rangle_s)$ in moderately dense gas-particle flows. Thus, the filtered drag force is estimated as

$$-\overline{\beta(\boldsymbol{u}_g - \boldsymbol{u}_s)} \approx -\frac{\widetilde{\beta}}{\overline{\epsilon}_s}\overline{\epsilon_s(\boldsymbol{u}_g - \boldsymbol{u}_s)} = \widetilde{\beta}(\langle \boldsymbol{u}_s \rangle_s - \langle \boldsymbol{u}_g \rangle_g - \boldsymbol{v}_d), \tag{40}$$

which is a good approximation of the filtered drag force [53,54]. Here, $\widetilde{\beta}$ is evaluated from filtered quantities, i.e., $\widetilde{\beta} = \beta(\overline{\epsilon}_s, \overline{\epsilon}_g, \langle \boldsymbol{u}_g \rangle_g, \langle \boldsymbol{u}_s \rangle_s)$. The turbulent interfacial work arising in the transport equation of gas-phase turbulent kinetic energy [51] is then expressed as a combination of drag-dissipation-and-exchange rate $\mathcal{DE}_g$ and drag production $\mathcal{DP}$ [38,51], as

$$\mathcal{DE}_g = \widetilde{\beta}(\langle \boldsymbol{u}_g''' \cdot \boldsymbol{u}_s'' \rangle_s - \langle \boldsymbol{u}_g''' \cdot \boldsymbol{u}_g''' \rangle_s), \tag{41}$$

$$\mathcal{DP} = \widetilde{\beta}\boldsymbol{v}_d(\langle \boldsymbol{u}_s \rangle_s - \langle \boldsymbol{u}_g \rangle_g), \quad \text{with} \quad \boldsymbol{v}_d = \langle \boldsymbol{u}_g \rangle_s - \langle \boldsymbol{u}_g \rangle_g. \tag{42}$$

In the turbulent kinetic energy equation of the solid phase, the turbulent interphase coupling raises only a drag-dissipation-and-exchange rate $\mathcal{DE}_s$ [51] written by

$$\mathcal{DE}_s = \widetilde{\beta}(\langle \boldsymbol{u}_g''' \cdot \boldsymbol{u}_s'' \rangle_s - \langle \boldsymbol{u}_s'' \cdot \boldsymbol{u}_s'' \rangle_s). \tag{43}$$

Equations (41) and (43) describe how kinetic energies on both are dissipated and exchanged between the phases by gas-solid velocity cross correlation. Equation (42) represents an additional turbulence

production on the gas phase generated by the drift velocity $\boldsymbol{v}_d$ and termed as drag production. This latter ($\boldsymbol{v}_d$) constitutes a measure of the subfilter gas-phase velocity fluctuations induced by the particle clustering and principally responsible for generating gas-phase turbulent kinetic energy. Now, employing the averaging identities of Germano [55], the (un)mixed averages appearing in the mesoscale work terms can be expanded as [51]

$$\langle \boldsymbol{u}_g''' \cdot \boldsymbol{u}_s'' \rangle_s = \langle \boldsymbol{u}_g \boldsymbol{u}_s \rangle_s - \langle \boldsymbol{u}_g \rangle_s \langle \boldsymbol{u}_s \rangle_s, \tag{44}$$

$$\langle \boldsymbol{u}_g''' \cdot \boldsymbol{u}_g''' \rangle_s = \langle \boldsymbol{u}_g \boldsymbol{u}_g \rangle_s - 2\langle \boldsymbol{u}_g \rangle_s \langle \boldsymbol{u}_g \rangle_g + \langle \boldsymbol{u}_g \rangle_g \langle \boldsymbol{u}_g \rangle_g, \tag{45}$$

$$\langle \boldsymbol{u}_s'' \cdot \boldsymbol{u}_s'' \rangle_s = \langle \boldsymbol{u}_s \boldsymbol{u}_s \rangle_s - \langle \boldsymbol{u}_s \rangle_s \langle \boldsymbol{u}_s \rangle_s. \tag{46}$$

Moreover, the drag coefficient $\widetilde{\beta}$ is evaluated upon the filtered variables, and by adopting the Wen and Yu [39] drag law

$$\widetilde{\beta} = \frac{3}{4}\widetilde{C}_D \frac{\overline{\epsilon}_g \overline{\epsilon}_s \rho_g \|\langle \boldsymbol{u}_g \rangle_g - \langle \boldsymbol{u}_s \rangle_s\|}{d_s} \overline{\epsilon}_g^{-2.65} \tag{47}$$

and

$$\widetilde{C}_D = \begin{cases} 24[1 + 0.15\widetilde{\mathrm{Re}}_s^{0.687}]/\widetilde{\mathrm{Re}}_s & \text{if} \quad \widetilde{\mathrm{Re}}_s < 1000 \\ 0.44 & \text{if} \quad \widetilde{\mathrm{Re}}_s \geqslant 1000 \end{cases} \quad \text{and,} \quad \widetilde{\mathrm{Re}}_s = \frac{\overline{\epsilon}_g \rho_g d_s \|\langle \boldsymbol{u}_g \rangle_g - \langle \boldsymbol{u}_s \rangle_s\|}{\mu_g}. \tag{48}$$

The idea is to map and sample the values of drag-dissipation-and-exchange rates and drag production, given by Eqs. (41), (42), and (43), in condition of JPDF (x_B, y_B) in BAM for the gas and solid phases, respectively. In other words, the average values of $\langle \mathcal{DE}_g | (x_B^g, y_B^g) \rangle$, $\langle \mathcal{DP} | (x_B^g, y_B^g) \rangle$, and $\langle \mathcal{DE}_s | (x_B^s, y_B^s) \rangle$, which are conditioned by the most probable JPDF of x_B and y_B, utilizing a filter length $\overline{\Delta} = 3\Delta$, are plotted and shown in Figs. 5(a), 5(b), and 5(c). The drag terms values are rendered by coloring and converged with a minimum sampling number about 400 in each bin-width coordinates in BAM. They are given in dimensionless form in terms of the terminal settling velocity u_t, ρ_s, and g, as the characteristic velocity, density, and acceleration [56] and the dimensional quantities for length u_t^2/g, time u_t/g, drag or stresses terms $\rho_s u_t g$, and the granular temperature u_t^2. Starting with the gas phase, the $\mathcal{DP}$ in Fig. 5(a) implies a preferential 1-D turbulence state favoring the gravity-aligned turbulent kinetic energy and the (relative) mean slip velocity, $\boldsymbol{v}_r = \langle \boldsymbol{u}_s \rangle_s - \langle \boldsymbol{u}_g \rangle_g$ [Eq. (42)]. Note that $\boldsymbol{v}_d$ and $\boldsymbol{v}_r$ are found to be directly (counter)aligned [33]; moreover, the magnitude of $\boldsymbol{v}_d$ was found to obey a vortex-sheet (2-D) turbulence complied on equivalent rotational and straining structures, i.e., balanced $Q_{\Omega_g} = -Q_{\mathrm{S}_g}$, where Q is the second invariant of rate-of-rotational Ω_g and rate-of-strain S_g gas-phase tensors [33]. Hence, this can explicate why the distribution of $\mathcal{DP}$ on BAM is skewed toward 2-D turbulence. The utmost (degenerate) values of $\mathcal{DE}_g$ in Fig. 5(b) follow exactly the same turbulence distribution of $\mathcal{DP}$ with an opposite negative sign. It indicates therewith the dominance of gas-phase turbulent kinetic energy seen by particles $\langle \boldsymbol{u}_g''' \cdot \boldsymbol{u}_g''' \rangle_s$ over the interacting cross-correlated turbulence between phases $\langle \boldsymbol{u}_g''' \cdot \boldsymbol{u}_s'' \rangle_s$. On the solid phase, the drag-dissipation-and-exchange rate $\mathcal{DE}_s$ plotted on BAM [Fig. 5(c)] shows, similarly, a 1-D turbulence preference to be fairly upturned (toward 3C) around its highest positive values. It might render with this shape the interfacial prolate-like turbulence around the clusters, whereas $\mathcal{DE}_s$ is totally negative inside the clusters. Because $\mathcal{DP}$ is vanished inside the clusters [Fig. 5(a)], the turbulent kinetic energy of the gas phase is not sufficiently high to support the turbulent kinetic energy on the solid phase, and hence $\mathcal{DE}_s$ is even negative, meaning that energy is dissipated due to the unresolved gas flow around the particles, where the momentum transfer is closed by a drag force. To get closer insight into this phenomenon, detailed particle-resolved DNS (PR-DNS) would be necessary, which resolves the flow around the particles, and a no-slip condition would be applied on the particle surface instead of using a drag correlation [57].

More interesting queries come to mind about how the interfacial turbulence changes spatially in different flow regions, e.g., from the dilute areas toward inside the clusters. Therefore, we retrieve
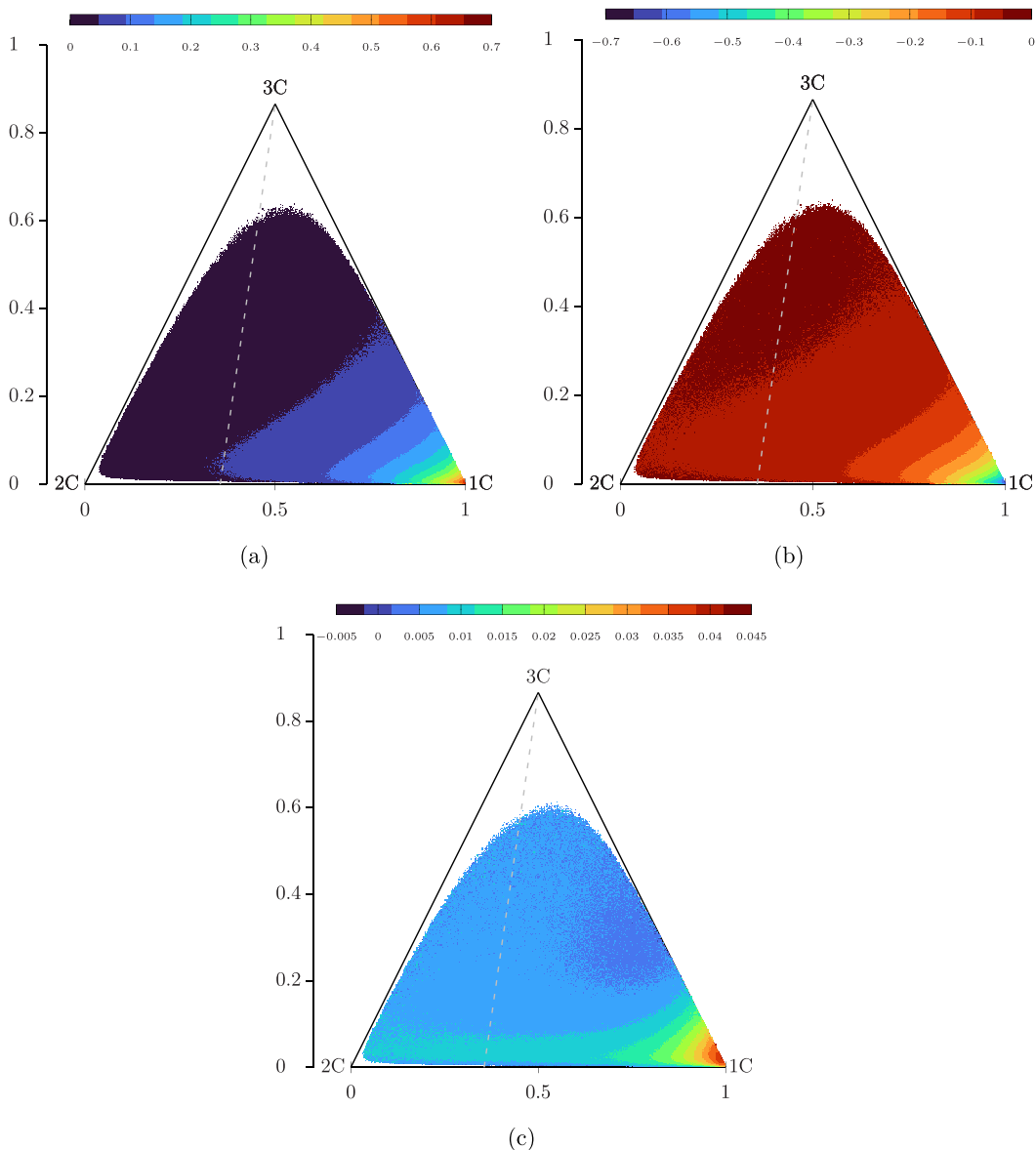
(a)

(b)

(c)

FIG. 5. Mean-ensemble values of (a) $\mathcal{DP}$, (b) $\mathcal{DE}_g$, and (c) $\mathcal{DE}_s$, normalized by $\rho_s u_t g$ and conditioned on (x_B, y_B) BAM using a filter length $\bar{\Delta} = 3\Delta$, for the TFM turbulent fluidization case.

the same turbulence trajectories constructed on gas and solid phase and previously unveiled in Figs. 3(b) and 3(c), respectively. They run in functional to $\bar{\epsilon}_s$, but now we color the points by the production values, $\mathcal{DP}$, $\mathcal{DE}_g$, and $\mathcal{DE}_s$. Namely, in each bin width of filtered solid volume fraction, we ensemble the coordinates $(\langle x_B | \bar{\epsilon}_s \rangle, \langle y_B | \bar{\epsilon}_s \rangle)$, to get the points trajectories in BAM, and we average the terms $\langle \mathcal{DE}_g | (x_B^g, y_B^g) | \bar{\epsilon}_s \rangle$, $\langle \mathcal{DP} | (x_B^g, y_B^g) | \bar{\epsilon}_s \rangle$, and $\langle \mathcal{DE}_s | (x_B^s, y_B^s) | \bar{\epsilon}_s \rangle$, in condition of those coordinates. Taking the turbulence trajectories filtered about $\bar{\Delta} = 6\Delta$, the coloring results for $\mathcal{DP}$, $\mathcal{DE}_g$, and $\mathcal{DE}_s$, are represented in Figs. 6(a), 6(b), and 6(c), respectively. It can be noted that the prevalent $\mathcal{DP}$ and $-\mathcal{DE}_g$ are, by logic, located in the interfacial areas ($\bar{\epsilon}_s$ around 0.35), which are classified as elongated pancake-like turbulence. They are clearly negligible in the dilute regions
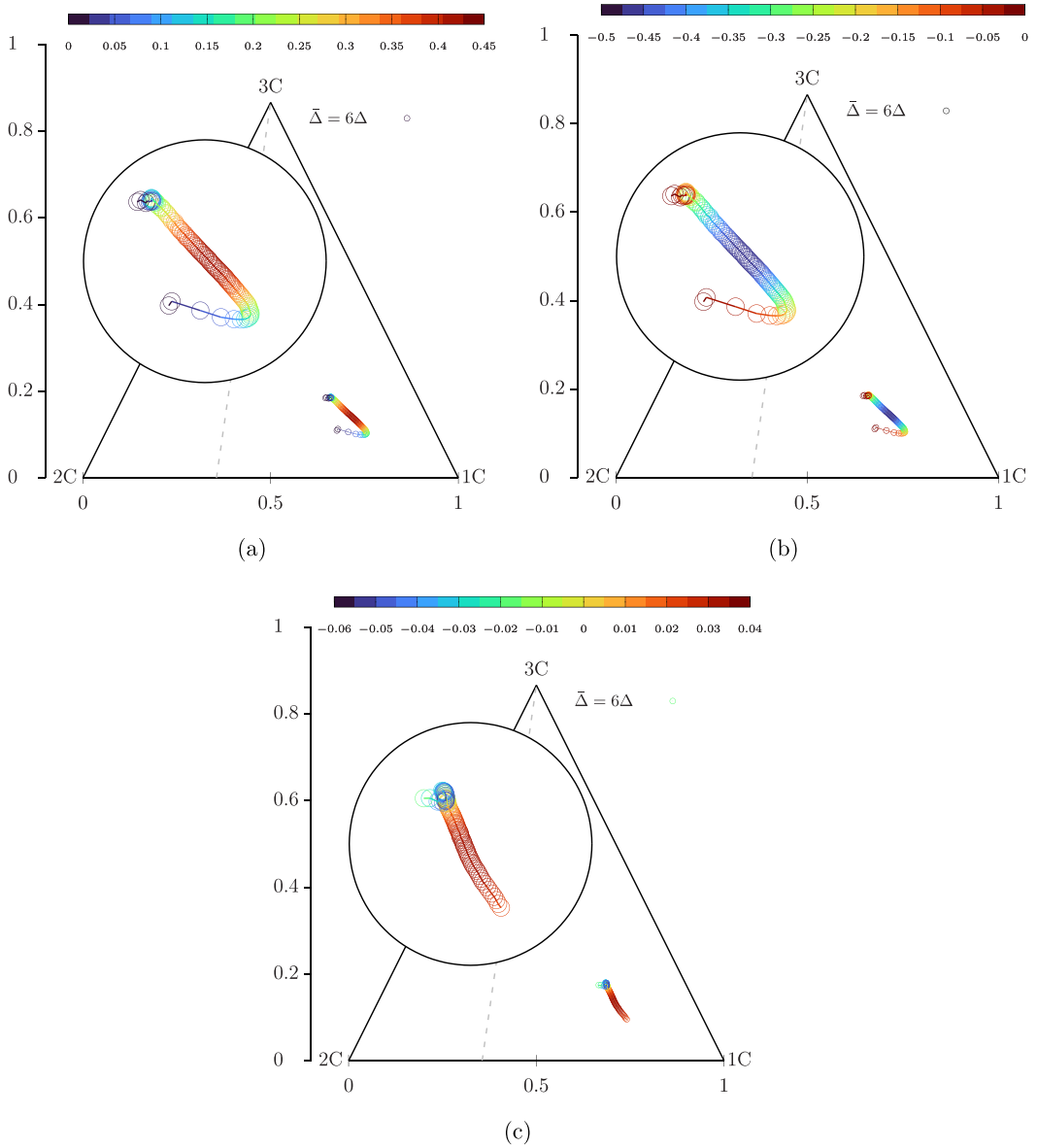
FIG. 6. The same turbulence trajectories taken from Fig. 3(b) on the gas phase and Fig. 3(c) on the solid one, at a filter length $\bar{\Delta} = 6\Delta$. They are plotted in (x_B, y_B) BAM constraint and in condition of $\bar{\epsilon}_s$, but colored by the mean-ensemble values of dimensionless (a) $\mathcal{DP}$, (b) $\mathcal{DE}_g$, and (c) $\mathcal{DE}_s$ (normalized by $\rho_s u_t g$). All trajectories are enlarged in a circle subset, and the data are taken from the TFM turbulent fluidization case.

and inside the clusters, since the phases are homogeneous there (e.g., no clusters, no drift velocity $\boldsymbol{v}_d = 0$, and no gas energy seen by solid, while moreover, variance solid concentration is zero inside the clusters). Correspondingly, the utmost solid-phase $\mathcal{DE}_s$ is similarly located in the interfacial areas, which are classified as prolate-like turbulence on solids, while $\mathcal{DE}_s$ becomes totally negative inside the clusters (as argued above).
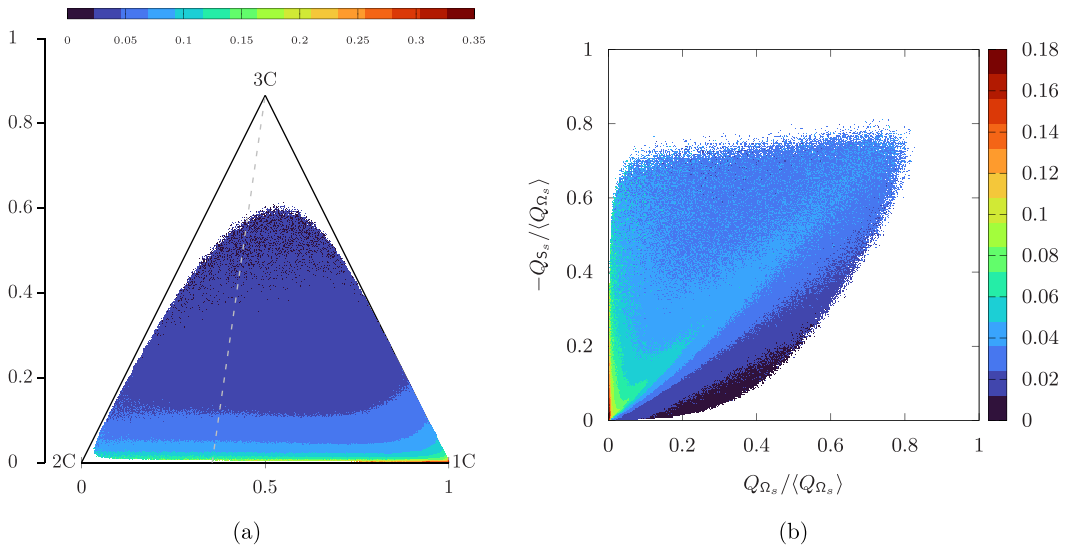
FIG. 7. (a) Mean-ensemble value of $\langle \Theta_s \rangle_s$, normalized by u_t^2 and conditioned on (x_B, y_B) BAM using a filter length $\bar{\Delta} = 3\Delta$. (b) represents the same mean-ensemble normalized magnitude of Θ_s conditioned on $(Q_{\Omega_s}, -Q_{S_s})$ invariant space. All data analyzed correspond to the TFM turbulent fluidization case.

V. GRANULAR TEMPERATURE

In the framework of TFM [34], the concept from the gas kinetic theory is used to describe the effective stresses of the solid phase resulting from particle-particle collisions and the translational dispersion of particles. Namely, by allowing an inelastic collision of particles, the Chapman-Enskog expansion is used to provide constitutive relations for the solid pressure tensor [17], which is decomposed into an isotropic contribution represented by the granular temperature Θ_s and the solid-phase viscous stress tensor [46]. The granular temperature Θ_s is introduced as a quantitative measure of the local uncorrelated particle fluctuations and defined as the residual component of the instantaneous particle velocity [46]. The total granular energy, then, discerns the difference between the (correlated) solid-phase turbulent kinetic energy $k_s = (1/2)\langle \mathbf{u}_s'' \cdot \mathbf{u}_s'' \rangle_s$ and the uncorrelated pseudo-thermal granular energy $(3/2)\langle \Theta \rangle_s$, as a sum of both, $k_s + (3/2)\langle \Theta \rangle_s$. Taking one third of the trace of solid pressure tensor [46], a balance equation of Θ_s transport is found and given in Table II [Eq. (9)]. In this context, we suggest inspecting the underlying turbulence states associated to $\langle \Theta_s \rangle_s$ by depicting its value in BAM, similar to that performed for the turbulent interfacial work in Fig. 5. It means that we evaluate $\langle \langle \Theta_s \rangle_s \rangle$ in condition of JPDF (x_B, y_B) in BAM on the solid phase and employ a filter length $\bar{\Delta} = 3\Delta$. Similar to the drag terms, the $\langle \Theta_s \rangle_s$ value is made dimensionless by u_t^2, and the resultant map is presented in Fig. 7(a). It can be seen that the highest granular temperature is located on 1-D turbulence preference with moderate nontrivial values expanded on the planar-like 2-D turbulence. This means that Θ_s avoids taking any prolate-like turbulence inside clusters or any oblate-like (pancake-like) turbulence, holding only linear and planar solid turbulence. In order to get an explanation, Θ_s is studied in the condition of the most probable JPDF $(Q_{\Omega_s}, -Q_{S_s})$, a space that provides important physical information about the dominant flow topologies with respect to the kinetic energy dissipation. Horizontal points inside $(Q_{\Omega_s}, -Q_{S_s})$ space indicate prevalent solid-body rotational structures, while vertical points represent irrotational straining domination. The points on the diagonal line portray a balanced enstrophy and dissipation $Q_{\Omega_s} = -Q_{S_s}$ occurring at vortex-sheet structures and 2-D boundary-layer-like turbulence. The JPDF map of $(Q_{\Omega_s}, -Q_{S_s})$ for moderately dense turbulent fluidization has been previously investigated on the base of a traceless weighted-phase velocity gradient tensors in our recent work [33]. Here, we
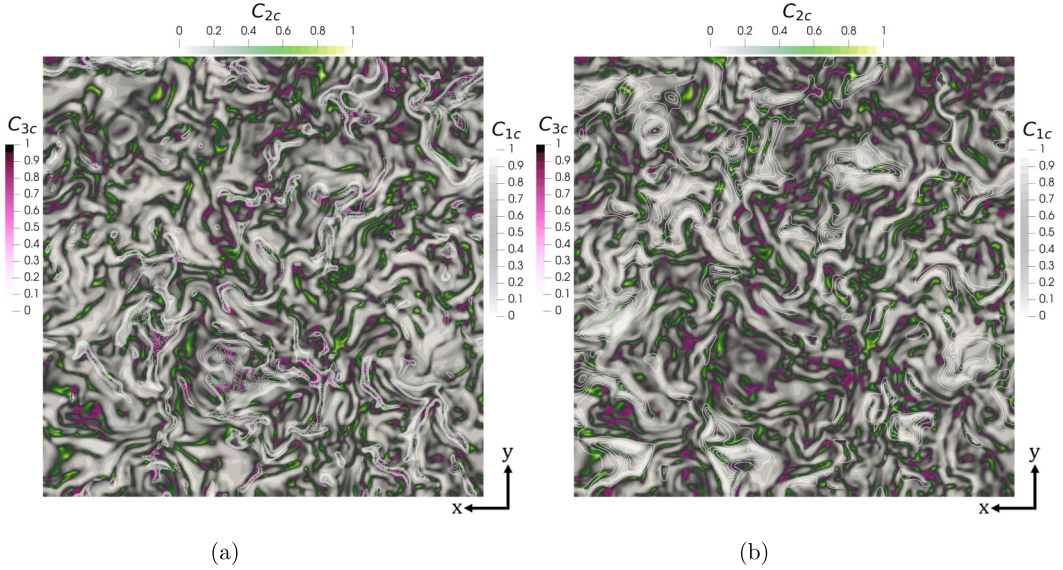
FIG. 8. Visualization of the three scalar metrics $\{1C, 2C, 3C\}$, computed on the solid-phase physical instantaneous domain with a filter length $\bar{\Delta} = 3\Delta$. The three scalar metrics $\{1C, 2C, 3C\}$, bounded between $[0,1]$, are rendered by three colors (gray, green-yellow, magenta), respectively, together with the isolines of highest $\langle \Theta_s \rangle_s$ (b) and clusters $\epsilon_s \in [0.3, 0.6]$ (a). Note that all representations are planar taken from the TFM turbulent fluidization case.

build the JPDF $(Q_{\Omega_s}, -Q_{S_s})$ map for the current turbulent fluidization case and print the averaged Θ_s value coloring in each bin-width space, as demonstrated in Fig. 7(b). It is worth noting that the utmost values of Θ_s are located on the large-scale irrotational solid strain-dominated slots, with a moderate distribution on the 2-D boundary-layer-like turbulence (diagonal). This picture agrees very well with BAM representation in Fig. 7(a) and leads to the conclusion that Θ_s obeys a prevalent 1-D turbulence in corresponding to the viscous shear straining solids.

To highlight the distribution of Θ_s in the context of turbulence anisotropy, a visualization of specific-point color triplets $\{1C, 2C, 3C\}$, which allows us to render turbulence states in physical domain, is built and shown in Figs. 8(a) and 8(b). Therein, we plot the three scalar metrics $\{1C, 2C, 3C\}$ [defined in Eqs. (34), (35), and (36), respectively] computed on the base of the solid-phase anisotropy stress tensor [Eq. (25)] and filter length $\bar{\Delta} = 3\Delta$, using three colors (gray, green-yellow, magenta). It thus permits the recognition of 1-D, 2-D isotropic, and 3-D turbulence positions on the solid-phase physical instantaneous domain. Furthermore, the contours of utmost $\langle \Theta_s \rangle_s$ in Fig. 8(b) and clusters $\bar{\epsilon}_s \in [0.3, 0.6]$ in Fig. 8(a) are rendered above as fine white lines. One can notice how the granular temperature places away from the clusters following preferential 1C turbulence and slight 2C turbulence, while the clusters tend to assemble in 3C turbulence (consistent with the trajectories observations).

Now, the question of why the granular temperature is moderately obeying the 2-D turbulence is still open. To resolve this query, we decide to analyze the principal terms on the right-hand side (RHS) of granular temperature transport equation [Eq. (9)], in the framework of BAM, precisely identical to $\langle \Theta_s \rangle_s$ in Fig. 7(a). Before that, it can be quite useful to investigate the impact of solid divergence $\nabla \cdot \boldsymbol{u}_s$ on both Θ_s and the three turbulence scalar metrics $\{1C, 2C, 3C\}$. Hence, for doing so, the ensemble PDF of Θ_s values in condition of each bin width $\nabla \cdot \boldsymbol{u}_s$, and $\{1C, 2C, 3C\}$ values in the bin widths $\overline{\nabla \cdot \boldsymbol{u}_s}$, are plotted together in Fig. 9(a). It is worth mentioning that the divergence solids, similar to Θ_s, are also considered dimensionless using the normalization quantity g/u_t. $\{1C, 2C, 3C\}$ have no dimension, and the solid divergence range is limited to $[-5, 5]$, which
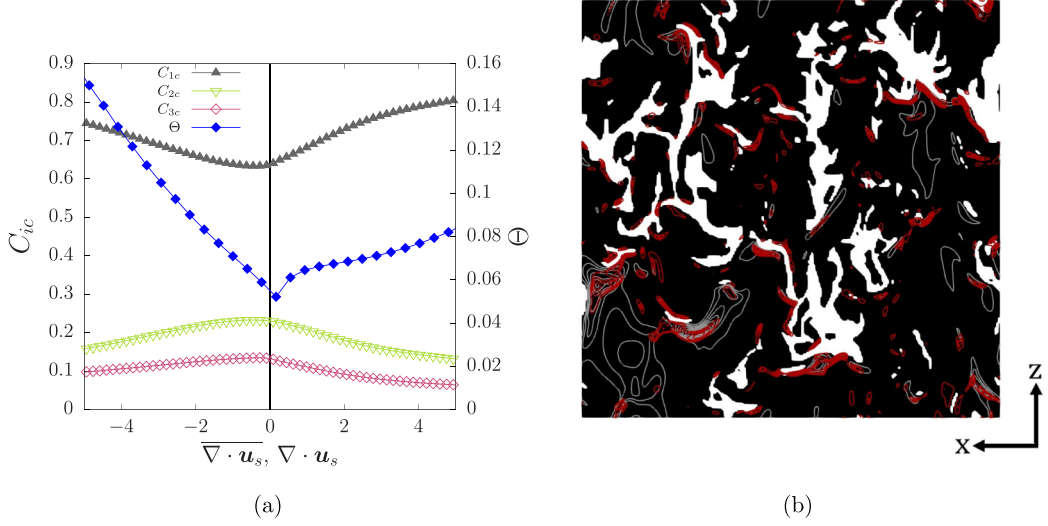
FIG. 9. (a) The ensemble PDF of normalized Θ_s in condition of $\nabla \cdot \boldsymbol{u}_s$, and {1C, 2C, 3C} values in condition of normalized $\overline{\nabla \cdot \boldsymbol{u}_s}$ using a filter length $\bar{\Delta} = 3\Delta$. The normalization quantity for divergence solids is g/u_t. (b) The contours of high Θ_s (gray lines), together with $-\nabla \cdot \boldsymbol{u}_s$ isolines (red lines) and clusters as white gaps. Note that the representation is planar, and all data are taken from the TFM turbulent fluidization case.

allows a good convergence of sampled terms. Interesting outcomes are obtained from Fig. 9(a): First, the granular temperature follows predominantly negative values of $\nabla \cdot \boldsymbol{u}_s$, which corresponds to a compressive heating of particle phase [46]. The maximum values of Θ_s comply with meaningful negative divergence magnitudes $-\nabla \cdot \boldsymbol{u}_s$ located at the upstream parts of clusters, as pictured in Fig. 9(b). Therein, Θ_s contours are drawn in gray lines, while the $-\nabla \cdot \boldsymbol{u}_s$ is rendered in red contours, together with the clusters viewed as white gaps. These findings agree rigorously with the observations reported by Capecelatro *et al.* [58]. Second, the peak magnitudes of 2C and 3C are mainly in negative divergence range ($\overline{\nabla \cdot \boldsymbol{u}_s} < 0$), while the utmost 1C tends to position toward positive divergence ($\overline{\nabla \cdot \boldsymbol{u}_s} > 0$) [Fig. 9(a)]. This can argue the 2-D turbulence nature of Θ_s distribution, driven by the negative divergence of solids $-\nabla \cdot \boldsymbol{u}_s$ and aligned to the upstream parts of falling clusters. Moreover, Θ_s holds the prevalent 1-D turbulence in association to the positive divergence $\nabla \cdot \boldsymbol{u}_s > 0$ dynamics, which truly corresponds to the shear straining solids (trace of S_s).

We return to the analysis of the principal terms appeared on the RHS of granular temperature balance equation [Eq. (9)], after applying a phase-averaged filter [Eq. (17)] with filter length $\bar{\Delta} = 3\Delta$ on the solid phase. First, the production of granular temperature due to viscous shear $\langle -\Sigma_s^{kc} : \nabla \boldsymbol{u}_s \rangle_s$ simplified to $\langle 2\mu_s^{kc}\mathsf{S}_s^d : \nabla \boldsymbol{u}_s \rangle_s$ is considered as an important heat source on the solid phase [46]. It can be split into two essential terms, the resolved production of $\langle \Theta_s \rangle_s$, i.e., $\overline{2\mu_s^{kc}\mathsf{S}_s^d} : \langle \nabla \boldsymbol{u}_s \rangle_s$, and the turbulent kinetic energy dissipation, i.e., $\langle 2\mu_s^{kc}\mathsf{S}_s^d : \nabla \boldsymbol{u}_s'' \rangle_s$, as [28,46]

$$\langle 2\mu_s^{kc}\mathsf{S}_s^d : \nabla \boldsymbol{u}_s \rangle_s = \overline{2\mu_s^{kc}\mathsf{S}_s^d} : \langle \nabla \boldsymbol{u}_s \rangle_s + \langle 2\mu_s^{kc}\mathsf{S}_s^d : \nabla \boldsymbol{u}_s'' \rangle_s. \tag{49}$$

Hence, we disclose the underlying turbulence states of the two elements in Eq. (49) by plotting them separately in BAM, precisely identical to $\langle \Theta_s \rangle_s$ in Fig. 7(a), as shown in Figs. 10(a) and 10(b). The magnitude of production terms therein are presented in dimensionless form (similar to drag terms Θ_s and divergence solid) using a normalization quantity $\rho_s u_t g$. From Fig. 10(a), the resolved production $\overline{2\mu_s^{kc}\mathsf{S}_s^d} : \langle \nabla \boldsymbol{u}_s \rangle_s$ exposes a clear 1-D turbulence preference which in turn conforms the previous conclusions, and thus the resolved shear dissipation stands to be the main source of the linear-like turbulent solid heating or granular temperature. The turbulent kinetic energy dissipation term in Fig. 10(b) shows a different distribution. It unveils a positive dominance in more prolate-like
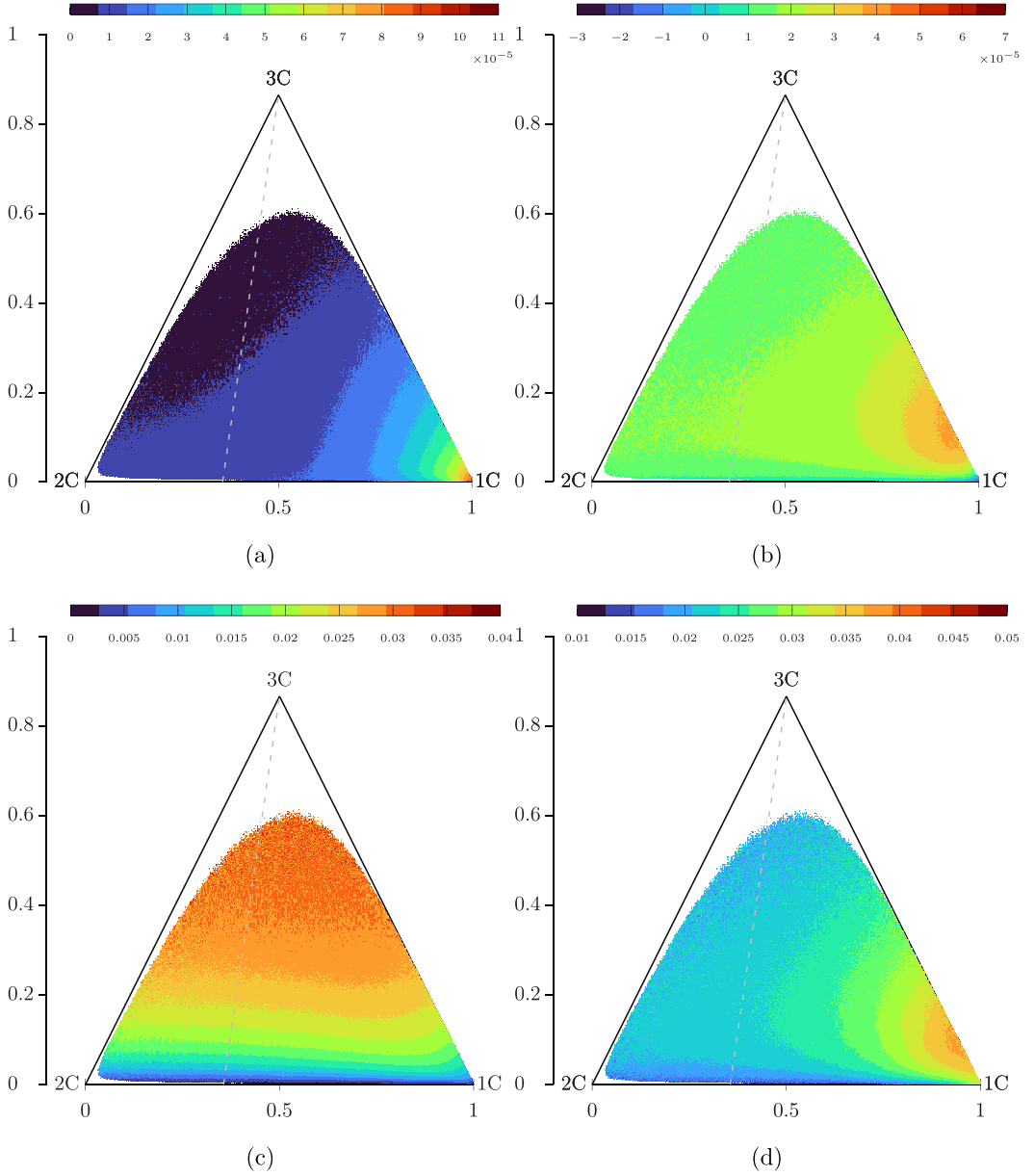
FIG. 10. Similar pictures to those presented in Figs. 5 and 7(a), but for (a) the resolved production $\overline{2\mu_s^{kc}\mathsf{S}_s^d}$: $\langle\nabla\boldsymbol{u}_s\rangle_s$, (b) the turbulent dissipation $\langle 2\mu_s^{kc}\mathsf{S}_s^d : \nabla\boldsymbol{u}_s''\rangle_s$, (c) the rate of $\langle\Theta_s\rangle_s$ production by gas-solid fluctuating slip $\langle\Gamma_s\rangle_s$, and (d) the dissipation due to viscous damping $\langle J_v\rangle_s$. All terms are normalized by $\rho_s u_t g$ with $\bar{\Delta} = 3\Delta$, for the TFM turbulent fluidization case.

turbulence, but a trivial negative weight in the turbulence state that supports $\langle\Theta_s\rangle_s$. It might be worthwhile to remark that the turbulent dissipation term $\langle 2\mu_s^{kc}\mathsf{S}_s^d : \nabla\boldsymbol{u}_s''\rangle_s$ appears in a negative sign on the RHS transport equation of solid-phase turbulent kinetic energy k_s [51] to dissipate k_s, but any negative contribution of it translates into a support of k_s. This might be argued and returned to the consideration of particles as a viscous solid [59], where the high collisions of particles might

produce the uncorrelated fluctuating dynamics that reflects Θ_s, to be correlated and supports k_s. Further investigations on this argument become important in the TFM framework.

The other two key elements in the $\langle\Theta_s\rangle_s$ transport equation are the dissipation due to viscous damping or inelastic particle-particle collisions $\langle J_v\rangle_s$ and the rate of $\langle\Theta_s\rangle_s$ production by gas-solid fluctuating slip $\langle\Gamma_s\rangle_s$. They are retrieved as

$$\Gamma_s = \frac{d_s\beta^2\|\boldsymbol{u}_g - \boldsymbol{u}_s\|^2}{4\epsilon_s g_0\rho_s\sqrt{\pi\Theta_s}}\Psi, \tag{50}$$

where

$$\Psi = \frac{R_d^2}{(1 + 3.5\epsilon_s^{1/2} + 5.9\epsilon_s)},$$

$$R_d = \begin{cases} \dfrac{1 + 3(\epsilon_s/2)^{1/2} + (135/64)\epsilon_s\ln\epsilon_s + 17.14\epsilon_s}{1 + 0.681\epsilon_s - 8.48\epsilon_s^2 + 8.16\epsilon_s^3}, & \epsilon_s < 0.4 \\ \dfrac{10\epsilon_s}{\epsilon_g^3} + 0.7, & \epsilon_s \geqslant 0.4 \end{cases}, \tag{51}$$

and

$$J_v = \frac{54\epsilon_s\mu_g\Theta_s}{d_s^2}R_{\text{diss}},$$
$$R_{\text{diss}} = 1 + \frac{3\epsilon_s^{1/2}}{\sqrt{2}} + \frac{135}{64}\epsilon_s\ln\epsilon_s + 11.26\epsilon_s\big(1 - 5.1\epsilon_s + 16.57\epsilon_s^2 - 21.77\epsilon_s^3\big) - \epsilon_s g_0\ln\epsilon_m, \tag{52}$$

where $\epsilon_m = 0.01$, as defined by Agrawal *et al.* [20] (Table II). We then plot the contributions $\langle\Gamma_s\rangle_s$ and $\langle J_v\rangle_s$ in the BAM constraint, normalized by $\rho_s u_t g$, at the same filter length $\bar{\Delta} = 3\Delta$, as displayed in Figs. 10(c) and 10(d), respectively. One can note that the production by slip $\langle\Gamma_s\rangle_s$ opposes the favoring turbulence states of $\langle\Theta_s\rangle_s$, whereas the viscous damping dissipation $\langle J_v\rangle_s$ conforms with the turbulent dissipation $\langle2\mu_s^{kc}\mathsf{S}_s^d : \nabla\boldsymbol{u}_s''\rangle_s$ anisotropy with a total positive sign. Since $\langle J_v\rangle_s$ seems to be dominant over $\langle\Gamma_s\rangle_s$ and appears negatively in Eq. (9), then it might balance or cancel the positive part of $\langle2\mu_s^{kc}\mathsf{S}_s^d : \nabla\boldsymbol{u}_s''\rangle_s$ leaving the resolved production $\overline{2\mu_s^{kc}\mathsf{S}_s^d} : \langle\nabla\boldsymbol{u}_s\rangle_s$ to be the main controller or source of granular temperature anisotropy preference.

VI. VARIANCE OF SOLID CONCENTRATION

The arrangements of particle clustering in statistically stationary homogeneous gravity-driven particulate flows stimulate volume-fraction and velocity fluctuations that appear as CIT or principal production component (drag production) for the gas-phase turbulent kinetic energy and Reynolds stresses [46]. This mechanism is quantified (as mentioned in Sec. IV) by the drift velocity, which can be expressed following Cloete *et al.* [60] as a function of the covariance of the solid volume fraction and the gas-phase velocity,

$$\boldsymbol{v}_d = \frac{\overline{\epsilon_s'\boldsymbol{u}_g'''}}{\overline{\epsilon}_s(1 - \overline{\epsilon}_s)}. \tag{53}$$

Then, it might be useful to investigate the underlying turbulence states associated to the drift velocity $\boldsymbol{v}_d$ [given inside Eq. (43) in its direct definition] in the framework of BAM. In order to decouple the $\boldsymbol{v}_d$ influence from the large-scale relative velocity $\boldsymbol{v}_r$, a normalized form is employed, reading as $\boldsymbol{v}_d \cdot \boldsymbol{v}_r/\|\boldsymbol{v}_r\|^2$ and plotted similarly to, e.g., the drag production $\mathcal{DP}$ [Fig. 5(a)], in Fig. 11(a). It shows the map of $\langle\boldsymbol{v}_d \cdot \boldsymbol{v}_r/\|\boldsymbol{v}_r\|^2\rangle$ with the condition of JPDF (x_B, y_B) in BAM on the gas phase using the (same) filter length $\bar{\Delta} = 3\Delta$. The (normalized) drift velocity thus implies a preferential 1-D turbulence state that solidly coincides with the drag production $\mathcal{DP}$ distribution. One can note how $\boldsymbol{v}_d$ is subtly obeying equivalent rotational and irrotational structures [33], translated into a
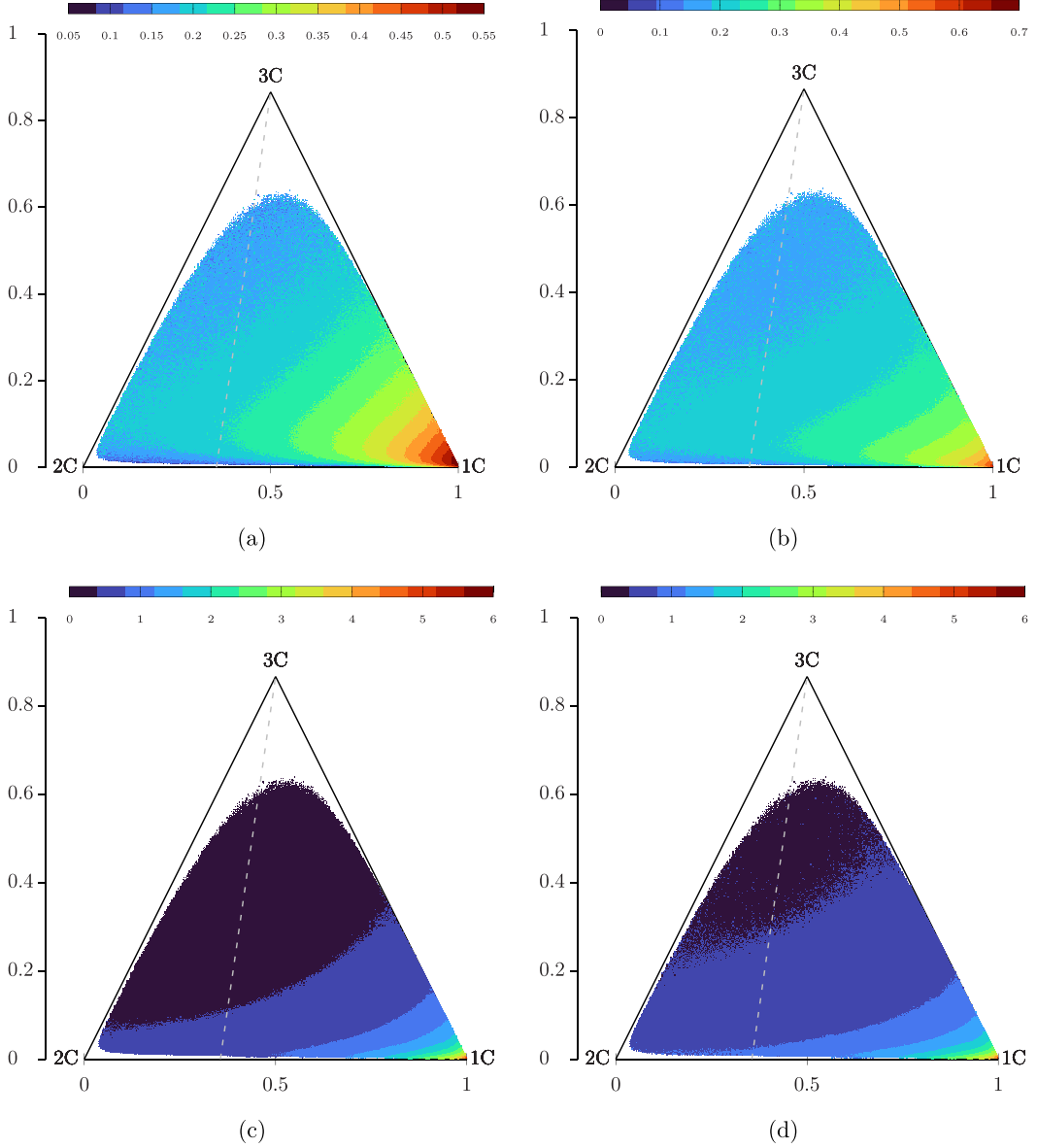
FIG. 11. Mean-ensemble values of (a) normalized drift velocity $\boldsymbol{v}_d \cdot \boldsymbol{v}_r / \|\boldsymbol{v}_r\|^2$, (b) variance of solid concentration $\overline{\epsilon_s'^2}/\overline{\epsilon_s}^2$, (c) $\|\langle \boldsymbol{u}_g''' \otimes \boldsymbol{u}_g''' \rangle_g\|$, and (d) $2k_g$ (Reynolds stresses magnitude and turbulent kinetic energy are normalized by u_t^2), conditioned on (x_B, y_B) BAM using a filter length $\bar{\Delta} = 3\Delta$, for the TFM turbulent fluidization case.

balanced linear-prolate and planar energy ellipsoids, and skewed toward 2-D turbulence. Taking the other definition of $\boldsymbol{v}_d$, deduced from Eq. (53), gives a rise to the variance or fluctuations of the solid concentration role in CIT and gas-phase turbulence. These solid fluctuations sustained by the clusters constitute the dominant gas-phase turbulence flux (by $\boldsymbol{v}_d$) and deserve to be explored in the background of turbulence type classification. Hence, we consider the variance of solid concentration (volume fraction) $\overline{\epsilon_s'^2} = \overline{\epsilon_s^2} - \overline{\epsilon_s}^2$ normalized by the large-scale concentration as, $\overline{\epsilon_s'^2}/\overline{\epsilon_s}^2$, in a way

similar to $\boldsymbol{v}_d \cdot \boldsymbol{v}_r / \|\boldsymbol{v}_r\|^2$. Interestingly, the distribution results of $\langle \overline{\epsilon_s'^2} / \bar{\epsilon}_s^2 \rangle$, rendered on the gas-phase BAM [Fig. 11(b)], show an identical 1-D turbulence preference as in $\boldsymbol{v}_d \cdot \boldsymbol{v}_r / \|\boldsymbol{v}_r\|^2$ and $\mathcal{DP}$. More precisely, it becomes closer to the drag production $\mathcal{DP}$ behavior, attesting to the strong and direct connection between the fluctuations of solid concentration and the dominant gas-phase turbulent kinetic energy production. In similar perspectives, the maps related to the gas-phase turbulent kinetic energy $2k_g$ and the magnitude of phase-filtered Reynolds stress tensor $\|\langle \boldsymbol{u}_g''' \otimes \boldsymbol{u}_g''' \rangle_g\|$ are inspected and displayed in Figs. 11(d) and 11(c), respectively. They are given in dimensionless form using u_t^2 and clearly indicate a (gravity-aligned) 1-D linear turbulence preference with a strong tendency to the planar-like 2-D turbulence. In a repetition to what previously reported in Sec. III, Figs. 11(c) and 11(d) give further evidence on the topological finding in Ref. [33], i.e., the preferential boundary-layer-like 2-D turbulence on the gas phase. Eventually, our current outcomes on $\overline{\epsilon_s'^2}$ and k_g relevant turbulence states promote the applicability of using these two terms in the estimation of the covariance of solid volume fraction and gas-phase velocity in drift velocity definition, Eq. (53). One example is the $\boldsymbol{v}_d$ model proposed by Rauchenzauner and Schneiderbauer [51] that assumes a closure of square root variance variables scaled by a linear correlation coefficient $\zeta_{\epsilon_s g}$, i.e.,

$$\boldsymbol{v}_d^{Rau} = \zeta_{\epsilon_s g} \frac{\sqrt{2k_g \overline{\epsilon_s'^2}}}{\bar{\epsilon}_s (1 - \bar{\epsilon}_s)}, \tag{54}$$

where $\zeta_{\epsilon_s g}$ is calculated dynamically using test filters [51]. Other drift velocity models are already available in literature [33,52,61,62], while the assessment of its performance inside the barycentric anisotropy map is out of the current paper's scope. It is worth noting from Figs. 11(c) and 11(d) how the weight of the gas-phase Reynolds stress tensor is fully controlled by its trace, i.e., turbulent kinetic energy anisotropy. Then let us compare, as well, the magnitude of the gas-phase rate-of-strain tensor in an analogous picture as $\|\langle \boldsymbol{u}_g''' \otimes \boldsymbol{u}_g''' \rangle_g\|$ [Fig. 11(c)]. Namely, we consider the filtered gas-phase rate-of-strain tensor $\bar{\mathsf{S}}_g = (1/2)(\bar{\mathsf{G}}_g + \bar{\mathsf{G}}_g^t)$, where $\bar{\mathsf{G}}_g = \nabla \langle \boldsymbol{u}_g \rangle_g$, and plot its magnitude $\|\bar{\mathsf{S}}_g\|$ in the framework BAM (same filter size and normalized by g/u_t), as represented in Fig. 12(b). It is compelling to see that the weight of resolved gas-phase rate-of-strain tensor is giving a similar distribution of turbulence anisotropy as the magnitude of phase-filtered Reynolds stress tensor and turbulent kinetic energy. This in turn encourages the applicability of eddy-viscosity assumption (Bossinesq hypothesis [49]), as a large-eddy simulation-type closure for the Reynolds stress contribution on the gas-phase turbulent fluidization, moderately dense cases, i.e.,

$$\langle \boldsymbol{u}_g''' \otimes \boldsymbol{u}_g''' \rangle_g \simeq \bar{\tau}_g = \tfrac{2}{3} \bar{\epsilon}_g k_g \mathsf{I} - 2\epsilon_g \nu_{tg} \left(\bar{\mathsf{S}}_g - \tfrac{1}{3} tr(\bar{\mathsf{S}}_g) \mathsf{I} \right). \tag{55}$$

Therein, the turbulent viscosity ν_{tg} can sympathetically be approached using a simple (dynamic) Smagorinsky model [49], $\nu_{tg} = (C_s \bar{\Delta})^2 (2\bar{\mathsf{S}}_g : \bar{\mathsf{S}}_g)^{1/2}$, or a Kolmogorov-Prandtl model [49], $\nu_{tg} = C_m \bar{\Delta} \bar{\epsilon}_g k_g^{1/2}$, where C_s and C_m are the model constants. Again, an example in this regard is the spatially averaged two-fluid model (SA-TFM) proposed by Schneiderbauer [63]. It used the Kolmogorov-Prandtl model in a mixing length assumption to close the Reynolds stress-like contributions on both gas and solid phases turbulence. We investigate the alignment trends of the eigenframe vectors imposed by our gas-phase filtered Reynolds stress and resolved rate-of-strain tensors (deviatoric parts). Recalling that both tensors are symmetric and second-order positive semi-definite matrices, they can thus be given in a decompositional canonical form in terms of eigenvalue and eigenvectors [similar to Eq. (27)] as $\bar{\tau}_g^d = \lambda_{\tau_1} \boldsymbol{\tau}_1 \boldsymbol{\tau}_1^t + \lambda_{\tau_2} \boldsymbol{\tau}_2 \boldsymbol{\tau}_2^t + \lambda_{\tau_3} \boldsymbol{\tau}_3 \boldsymbol{\tau}_3^t$ and $\bar{\mathsf{S}}_g^d = \lambda_{s_1} \boldsymbol{s}_1 \boldsymbol{s}_1^t + \lambda_{s_2} \boldsymbol{s}_2 \boldsymbol{s}_2^t + \lambda_{s_3} \boldsymbol{s}_3 \boldsymbol{s}_3^t$, respectively. The eigenvectors' strain-stress alignments are then computed and revealed in Fig. 12(a) to show consistent observations with those reported in the literature for isotropic turbulence [64]. For instance, the same relative preferred orientation of 45 deg for the most extensional $\boldsymbol{\tau}_1 \cdot \boldsymbol{s}_1$ and contracting $\boldsymbol{\tau}_3 \cdot \boldsymbol{s}_3$ eigenvectors, and the perfect parallel orientation for the principal intermediate $\boldsymbol{\tau}_2 \cdot \boldsymbol{s}_2$ eigenvectors, are recaptured here (on the gas-phase turbulence). In the end, our aim behind is only to demonstrate the motivation of applying eddy-viscosity models
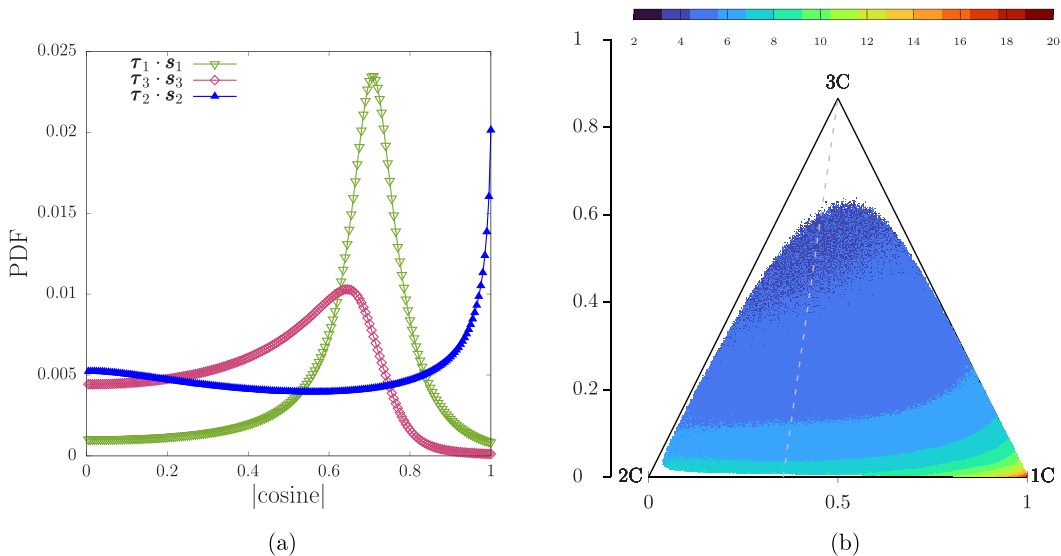
FIG. 12. (a) PDFs of the direction cosines between the eigenvectors of $\bar{\tau}_g^d$ and $\bar{S}_g^d$. (b) Mean-ensemble values of magnitude gas-phase rate-of-strain tensor, similar to Fig. 11, and normalized by g/u_t on (x_B, y_B) BAM using a filter length $\bar{\Delta} = 3\Delta$ for the TFM turbulent fluidization case.

for Reynolds stress-like contribution in turbulent fluidization, not discuss the alignment outcomes. Similar to the drift velocity above, any *a posteriori* assessment (or even *a priori*) of Reynolds stress models utilizing the barycentric anisotropy map is out of this paper's scope.

VII. CONCLUSIONS

In this work, the turbulence anisotropy in moderately dense turbulent fluidization is characterized with the aid of the barycentric anisotropy map (BAM) [6]; such a critical space based on the convex combination of scalar metrics dependent on eigenvalues of the phase-filtered anisotropy stress tensors. These latter are defined as the deviatoric (traceless) part of the phase-averaged Reynolds stress tensors normalized by twice the phasic turbulent kinetic energies. The BAM has provided a nondistorted visual representation of turbulence anisotropy on an equilateral triangle. It conveys information on the orientation of turbulence and the weighting of anisotropy [6], in terms of three limiting states, one-component (1-D turbulence), two-component (2-D isotropic turbulence), and three-component (3-D isotropic turbulence). The data set for analysis was obtained from a highly resolved kinetic theory-based TFM simulation, performed for fully triply periodic (unbounded) cubic domain of moderately dense turbulent fluidization (Geldart A particles). The predominant turbulence state identified on the JPDF map of (x_B, y_B) BAM coordinates has indicated a 1-D turbulence type on both phases. It manifests on the dominant streamwise turbulent kinetic energy component, which generates turbulence anisotropy in gravity-driven cluster-induced turbulence. The turbulence trajectories, on the other hand, altering upon different flow regimes from dilute areas toward inside the clusters, are investigated in the framework of BAM on both phases. They have revealed, on the gas phase, a prevalent 2-D ellipse-like turbulence in the dilute regions, changing to 1-D turbulence in transition areas, and tend toward 3-D turbulence in elongated pancake-like turbulence at the interface and inside the clusters. On the solid phase, the trajectories have implied a shorter change from 1-D linear turbulence in transition areas toward prolate-like 3-D turbulence at the interface and inside the clusters. The turbulence evolution is investigated considering the temporal trajectories in BAM, yielding insights into the turbulence decay in the aspect of return-to-isotropy rate [49]. The turbulence trajectories on the solid phase have shown a demarcation line that

isolates the evolution of the prolate-like cluster's turbulence from the development of oblate-like or planar-like background solid strain. However, the trajectories on the gas phase are found to rotate, altering any near prolate-like turbulence driven by clusters to a 1-D turbulence, which is then developed into 2-D turbulence toward disk-like or pancake-like structure. In the same BAM framework of the JPDF and spatial turbulence trajectories maps, the turbulence anisotropy of turbulent interfacial work, cluster-induced turbulence (CIT), and the granular temperature, which is defined as a measure of pseudo-thermal energy produced by uncorrelated particles agitation, have been inspected. The 1-D turbulence preference has been reported for all effective drag-dissipation-and-exchange rates and drag production. The maximum gas-phase drag magnitudes are found to hold an interfacial elongated pancake-like turbulence, while it becomes fairly upturned on the solid phase, to obey more prolate-like interfacial turbulence. In further analysis, the granular temperature $\langle \Theta_s \rangle_s$ indicates 1-D turbulence preference in association with the resolved solid strain dissipation (resolved production of $\langle \Theta_s \rangle_s$) and positive solid divergence; moreover, it is found to obey moderately a 2-D turbulence nature under the impact of negative solid divergence, aligned preferentially to the upstream parts of falling clusters. To complete the study, the variance of solid concentration which is principally produced by the clusters is analyzed on the BAM framework, together with the drift velocity, the gas-phase turbulent kinetic energy, and the magnitude of the same phase Reynolds stress and rate-of-strain tensors. Interestingly, the solid variance has shown an identical distribution to the drag production, similar to the underlying turbulence anisotropy of the drift velocity and the gas-phase turbulent kinetic energy. They all favor the 1-D linear turbulence with a strong tendency to the planar-like 2-D turbulence. This in turn has encouraged the applicability of using the variance solid concentration and the gas-phase turbulent kinetic energy in the modeling closure of the subgrid drift velocity. The similar behavior of gas-phase magnitude Reynolds stress and rate-of-strain tensors on BAM has promoted, as well, the valid use of eddy-viscosity assumption as an appropriate model for Reynolds stress contribution on the gas-phase turbulence.

These findings eventually enrich our understanding of turbulence anisotropy in turbulent fluidization, being a reference to building better second-moments models, e.g., for the Reynolds stresses, that can be analytically assessed inside the barycentric anisotropy map. This last will constitute our primary concern in the future.

[1] K. Choi and J. Lumley, The return to isotropy of homogeneous turbulence, J. Fluid Mech. **436**, 59 (2001).

[2] S. Schneiderbauer and M. Saeedipour, The impact of interphase forces on the modulation of turbulence in multiphase flows, Acta Mech. Sin. **38**, 721446 (2022).

[3] P. Gualtieri, F. Picano, G. Sardina, and C. M. Casciola, Clustering and turbulence modulation in particle-laden shear flows, J. Fluid Mech. **715**, 134 (2013).

[4] J. Rotta, Statistische Theorie nichthomogener Turbulenz, Z. Phys. **129**, 547 (1951).

[5] L. J. Lumley and G. R. Newman, The return to isotropy of homogeneous turbulence, J. Fluid Mech. **82**, 161 (1977).

[6] S. Banerjee, R. Krahl, F. Durst, and Ch. Zenger, Presentation of anisotropy properties of turbulence, invariants versus eigenvalue approaches, J. Turbul. **8**, N32 (2007).

[7] J. L. Lumley, Computational modeling of turbulent flows, Adv. Appl. Mech. **18**, 123 (1978).

[8] L. Terentiev, The turbulence closure model based on linear anisotropy invariant analysis, Ph.D. thesis, Technische Fakultät der Universität Erlangen-Nürnberg, Germany, 2005.

[9] G. Emory and G. Iaccarino, Visualizing turbulence anisotropy in the spatial domain with componentality contours, Center for Turbulence Research, Annual Research Briefs, 2014, pp. 123–138.

[10] I. Stiperski, G. G. Katul, and M. Calaf, Universal Return-to-Isotropy of Inhomogeneous Atmospheric Boundary Layer Turbulence, Phys. Rev. Lett. **126**, 194501 (2021).

[11] G. Iaccarino, A. A. Mishra, and S. Ghili, Eigenspace perturbations for uncertainty estimation of single-point turbulence closures, Phys. Rev. Fluids **2**, 024605 (2017).

[12] A. A. Mishra and G. Iaccarino, Theoretical analysis of tensor perturbations for uncertainty quantification of Reynolds averaged and subgrid scale closures, Phys. Fluids **31**, 075101 (2019).

[13] J. F. Heyse, A. A. Mishra, and G. Iaccarino, Estimating RANS model uncertainty using machine learning, J. Global Power Propulsion Soc. 1 (2021).

[14] K. Nobarani and S. E. Razavi, Deep learning to advance the eigenspace perturbation method for turbulence model uncertainty quantification, arXiv:2202.12378.

[15] M. Andersson and M. Karlsson, Characterization of anisotropic turbulence behavior in pulsatile blood flow, Biomech. Model. Mechanobiol. **20**, 491 (2021).

[16] T. Ma, B. Ott, J. Fröhlich, and A. D. Bragg, Scale-dependent anisotropy, energy transfer, and intermittency in bubble-laden turbulent flows, J. Fluid Mech. **927**, A16 (2021).

[17] C. K. K. Lun, S. B. Savage, D. J. Jeffrey, and N. Chepurniy, Kinetic theories for granular flow: Inelastic particles in Couette flow and slightly inelastic particles in a general flow field, J. Fluid Mech. **140**, 223 (1984).

[18] D. Gidaspow, *Multiphase Flow and Fluidization* (Academic Press, San Diego, 1994).

[19] T. B. Anderson and R. Jackson, Fluid mechanical description of fluidized beds. Equations of motion, Ind. Eng. Chem. Fund. **6**, 527 (1967).

[20] K. Agrawal, P. N. Loezos, M. Syamlal, and S. Sundaresan, The role of meso-scale structures in rapid gas-solid flows, J. Fluid Mech. **445**, 151 (2001).

[21] W. D. Fullmer and C. M. Hrenya, Quantitative assessment of fine-grid kinetic-theory-based predictions of mean-slip in unbounded fluidization, AIChE J. **62**, 11 (2016).

[22] W. D. Fullmer, G. Liu, X. Yin, and C. M. Hrenya, Clustering instabilities in sedimenting fluid-solid systems: Critical assessment of kinetic-theory-based predictions using direct numerical simulation data, J. Fluid Mech. **823**, 433 (2017).

[23] M. C. Baker, R. O. Fox, B. Kong, J. Capecelatro, and O. Desjardins, Reynolds-stress modeling of cluster-induced turbulence in particle-laden vertical channel flow, Phys. Rev. Fluids **5**, 074304 (2020).

[24] R. O. Fox, On multiphase turbulence models for collisional fluid-particle flows, J. Fluid Mech. **742**, 368 (2014).

[25] S. Beetham, R. O. Fox, and J. Capecelatro, Sparse identification of multiphase turbulence closures for coupled fluid-particle flows, J. Fluid Mech. **914**, A11 (2021).

[26] A. Innocenti, R. O. Fox, and S. Chibbaro, A Lagrangian probability-density-function model for turbulent particle-laden channel flow in the dense regime, Phys. Fluids **33**, 053308 (2021).

[27] A. M. Lattanzi, V. Tavanashad, S. Subramaniam, and J. Capecelatro, Stochastic model for the hydrodynamic force in Euler-Lagrange simulations of particle-laden flows, Phys. Rev. Fluids **7**, 014301 (2022).

[28] S. Rauchenzauner and S. Schneiderbauer, A dynamic multiphase turbulence model for coarse-grid simulations of fluidized gas-particle suspensions, Chem. Eng. Sci. **247**, 117104 (2022).

[29] S. Schneiderbauer and M. Saeedipour, Sub-grid deconvolution approach for filtered two-fluid models and the application to fluidized gas-particle suspensions, in *Turbulence and Interactions* (Springer International, Berlin, 2021), pp. 183–188.

[30] S. Schneiderbauer and M. Saeedipour, Numerical simulation of turbulent gas-solid flow using an approximate deconvolution model, Int. J. Multiphase Flow **114**, 287 (2019).

[31] S. Schneiderbauer, Validation study on spatially averaged two-fluid model for gas-solid flows: I. *a priori* analysis of wall bounded flows, AIChE J. **64**, 1591 (2018).

[32] M. H. Uddin and C. J. Coronella, Effects of grid size on predictions of bed expansion in bubbling fluidized beds of Geldart B particles: A generalized rule for a grid-independent solution of TFM simulations, Particuology **34**, 61 (2017).

[33] F. Dabbagh and S. Schneiderbauer, Small-scale flow topologies, pseudo-turbulence, and impact on filtered drag models in turbulent fluidization, Phys. Rev. Fluids **6**, 074301 (2021).

[34] B. G. M. van Wachem, J. C. Schouten, C. M. van den Bleek, R. Krishna, and J. L. Sinclair, Comparative analysis of CFD models of dense gas-solid systems, AIChE J. **47**, 1035 (2001).

[35] S. Schneiderbauer, A. Aigner, and S. Pirker, A comprehensive frictional-kinetic model for gas-particle flows: Analysis of fluidized and moving bed regimes, Chem. Eng. Sci. **80**, 279 (2012).

[36] N. P. Waterson and H. Deconinck, Design principles for bounded higher-order convection schemes—a unified approach, J. Comput. Phys. **224**, 182 (2007).

[37] Openfoam v5 user guide, Op (2018)en FOAM Foundation https://cfd.direct/openfoam/user-guide-v5/.

[38] J. Capecelatro, O. Desjardins, and R. O. Fox, On the transition between turbulence regimes in particle-laden channel flows, J. Fluid Mech. **845**, 499 (2018).

[39] C. Y. Wen and Y. H. Yu, Mechanics of fluidization, Chem. Eng. Prog. Symp. Ser. **62**, 100 (1966).

[40] Y. Igci, A. T. Andrews, S. Sundaresan, S. Pannala, and T. J. O'Brien, Filtered two-fluid models for fluidized gas-particle suspensions, AIChE J. **54**, 1431 (2008).

[41] S. Radl and S. Sundaresan, A drag model for filtered Euler-Lagrange simulations of clustered gas-particle suspensions, Chem. Eng. Sci. **117**, 416 (2014).

[42] M. Ishii, *Thermo-Fluid Dynamic Theory of Two-Phase Flow*, Collection de la Direction des Etudes et recherches d'Electricité de France (Eyrolles, Paris, 1975).

[43] U. Schumann, Realizability of Reynolds-stress turbulence models, Phys. Fluids **20**, 721 (1977).

[44] G. Kindlmann, Superquadric tensor glyphs, in *Proceedings of the 6th Joint Eurographics-IEEE TCVG Conference on Visualization* (Eurographics Association, Konstanz, Germany, 2004), pp. 147–154.

[45] W. N. Edeling, G. Iaccarino, and P. Cinnella, Data-free and data-driven RANS predictions with quantified uncertainty, Flow, Turbul. Combust. **100**, 593 (2018).

[46] J. Capecelatro, O. Desjardins, and R. O. Fox, On fluid-particle dynamics in fully developed cluster-induced turbulence, J. Fluid Mech. **780**, 578 (2015).

[47] W. D. Fullmer and C. M. Hrenya, Continuum prediction of scale-dependent, anisotropic fluctuating kinetic energy in gas-solid flows, Chem. Eng. Sci. **186**, 84 (2018).

[48] A. Ferrante and S. Elghobashi, On the physical mechanisms of two-way coupling in particle-laden isotropic turbulence, Phys. Fluids **15**, 315 (2003).

[49] S. B. Pope, *Turbulent Flows* (Cambridge University Press, Cambridge, UK, 2000).

[50] S. Sarkar and C. G. Speziale, A simple nonlinear model for the return to isotropy in turbulence, Phys. Fluids A: Fluid Dyn. **2**, 84 (1990).

[51] S. Rauchenzauner and S. Schneiderbauer, A dynamic anisotropic spatially averaged two-fluid model for moderately dense gas-particle flows, Int. J. Multiphase Flow **126**, 103237 (2020).

[52] J.-F. Parmentier, O. Simonin, and O. Delsart, A functional subgrid drift velocity model for filtered drag prediction in dense fluidized bed, AIChE J. **58**, 1084 (2012).

[53] S. Schneiderbauer and M. Saeedipour, Approximate deconvolution model for the simulation of turbulent gas-solid flows: An *a priori* analysis, Phys. Fluids **30**, 023301 (2018).

[54] A. Ozel, Y. Gu, C. C. Milioli, J. Kolehmainen, and S. Sundaresan, Towards filtered drag force model for non-cohesive and cohesive particle-gas flows, Phys. Fluids **29**, 103308 (2017).

[55] M. Germano, Turbulence: The filtering approach, J. Fluid Mech. **238**, 325 (1992).

[56] Y. Igci and S. Sundaresan, Verification of filtered two-fluid models for gas-particle flows in risers, AIChE J. **57**, 2691 (2011).

[57] M. Mehrabadi, J. A. K. Horwitz, S. Subramaniam, and A. Mani, A direct comparison of particle-resolved and point-particle methods in decaying turbulence, J. Fluid Mech. **850**, 336 (2018).

[58] J. Capecelatro, O. Desjardins, and R. O. Fox, Numerical study of collisional particle dynamics in cluster-induced turbulence, J. Fluid Mech. **747**, R2 (2014).

[59] C. M. Hrenya and J. L. Sinclair, Effects of particle-phase turbulence in gas-solid flows, AIChE J. **43**, 853 (1997).

[60] J. H. Cloete, S. Cloete, S. Radl, and S. Amini, On the choice of closure complexity in anisotropic drag closures for filtered two fluid models, Chem. Eng. Sci. **207**, 379 (2019).

[61] A. Ozel, P. Fede, and O. Simonin, Development of filtered Euler-Euler two-phase model for circulating fluidised bed: High resolution simulation, formulation, and *a priori* analyses, Int. J. Multiphase Flow **55**, 43 (2013).

[62] A. D. Burns, T. Frank, I. Hamill, and J. Shi, The Favre averaged drag model for turbulent dispersion in Eulerian multi-phase flows, in *5th International Conference on Multiphase Flow, ICMF'04* (Yokohama, Japan, May. Proceeding CD-ROM, 2004), paper No. 392, pp. 1–17.

[63] S. Schneiderbauer, A spatially-averaged two-fluid model for dense large-scale gas-solid flows, AIChE J. **63**, 3544 (2017).

[64] K. Horiuti, Alignment of eigenvectors for strain rate and subgrid-scale stress tensors, in *Direct and Large-Eddy Simulation IV* (Springer, Berlin, 2001), pp. 67–72.